EP 250108a/SN 2025kg: Observations of the most nearby Broad-Line Type Ic Supernova Following an Einstein Probe Fast X-ray Transient

Jillian C. Rastinejad,[1] Andrew J. Levan,[2,3] Peter G. Jonker,[2] Charles D. Kilpatrick,[1] Christopher L. Fryer,[4] Nikhil Sarin,[5,6] Benjamin P. Gompertz,[7,8] Chang Liu,[1] Rob A. J. Eyles-Ferris,[9] Wen-fai Fong,[1] Eric Burns,[10] James H. Gillanders,[11] Ilya Mandel,[12,13] Daniele Bjørn Malesani,[14,15] Paul T. O'Brien,[9] Nial R. Tanvir,[9] Kendall Ackley,[3] Amar Aryan,[16] Franz E. Bauer,[17] Steven Bloemen,[2] Thomas de Boer,[18] Clécio R. Bom,[19] Jennifer A. Chacón,[20,21] Ken Chambers,[18] Ting-Wan Chen,[16] Ashley A. Chrimes,[2,22] Joyce N. D. van Dalen,[2] Valerio D'Elia,[23] Massimiliano De Pasquale,[24] Michael D. Fulton,[25] Paul J. Groot,[2,26,27] Rahul Gupta,[28,*] Dieter H. Hartmann,[29] Agnes P.C. van Hoof,[2] Mark E. Huber,[18] Luca Izzo,[30,31] Wynn Jacobson-Galan,[32,†] Páll Jakobsson,[33] Albert Kong,[34] Tanmoy Laskar,[35,2] Thomas B. Lowe,[36] Eugene A. Magnier,[37] Elisabetta Maiorano,[38] Antonio Martin-Carrillo,[39] Lluis Mas-Ribas,[40,41] Daniel Mata Sánchez,[42,43] Matt Nicholl,[25] Christopher J. Nixon,[44] Samantha R. Oates,[45] Gregory Paek,[18] Jesse Palmerio,[46] Diego Paris,[47] Daniëlle L. A. Pieterse,[2] Giovanna Pugliese,[48] Jonathan A. Quirola Vasquez,[2] Jan van Roestel,[49] Andrea Rossi,[38] Alicia Rouco Escorial,[22] Ruben Salvaterra,[50] Benjamin Schneider,[51] Stephen J. Smartt,[11,25] Ken Smith,[11,25] Ian A. Smith,[18] Shubham Srivastav,[11] Manuel A. P. Torres,[42,43] Chiara Ventura,[47] Paul Vreeswijk,[2] Richard Wainscoat,[18] Yi-Jung Yang,[16] and Sheng Yang[52]

[1]Center for Interdisciplinary Exploration and Research in Astrophysics (CIERA) and Department of Physics and Astronomy, Northwestern University, Evanston, IL 60208, USA

[2]Department of Astrophysics/IMAPP, Radboud University, 6525 AJ Nijmegen, The Netherlands

[3]Department of Physics, University of Warwick, Coventry, CV4 7AL, UK

[4]Center for Nonlinear Studies, Los Alamos National Laboratory, Los Alamos, NM 87545 USA

[5]The Oskar Klein Centre, Department of Physics, Stockholm University, AlbaNova, Stockholm, SE-106 91, Stockholm, Sweden

[6]Nordita, Stockholm University and KTH Royal Institute of Technology, Hannes Alfvéns väg 12, Stockholm, SE-106 91, Stockholm, Sweden

[7]School of Physics and Astronomy, University of Birmingham, Birmingham B15 2TT, UK

[8]Institute for Gravitational Wave Astronomy, University of Birmingham, Birmingham B15 2TT

[9]School of Physics and Astronomy, University of Leicester, University Road, Leicester, LE1 7RH, UK

[10]Department of Physics and Astronomy, Louisiana State University, Baton Rouge, Louisiana 70803, USA

[11]Astrophysics sub-Department, Department of Physics, University of Oxford, Keble Road, Oxford, OX1 3RH, UK

[12]School of Physics and Astronomy, Monash University, Clayton VIC 3800, Australia

[13]ARC Centre of Excellence for Gravitational-wave Discovery (OzGrav), Melbourne, Australia

[14]Cosmic Dawn Center (DAWN), Denmark

[15]Niels Bohr Institute, University of Copenhagen, Jagtvej 128, Copenhagen, 2200, Denmark

[16]Graduate Institute of Astronomy, National Central University, 300 Jhongda Road, 32001 Jhongli, Taiwan

[17]Instituto de Alta Investigación, Universidad de Tarapacá, Casilla 7D, Arica, Chile

[18]Institute for Astronomy, University of Hawaii, 2680 Woodlawn Drive, Honolulu, HI 96822, USA

[19]Centro Brasileiro de Pesquisas Físicas, Rua Dr. Xavier Sigaud 150, 22290-180 Rio de Janeiro, RJ, Brazil

[20]Instituto de Astrofísica, Facultad de Física, Pontificia Universidad Católica de Chile, Campus San Joaquín, Av. Vicuña Mackenna 4860, Macul Santiago, Chile, 7820436

[21]Millennium Institute of Astrophysics, Nuncio Monseñor Sótero Sanz 100, Of 104, Providencia, Santiago, Chile

[22]European Space Agency (ESA), European Space Astronomy Centre (ESAC), Camino Bajo del Castillo s/n, 28692 Villanueva de la Cañada, Madrid, Spain

[23]Space Science Data Center (SSDC) - Agenzia Spaziale Italiana (ASI), I-00133 Roma, Italy

[24]Department of Mathematics and Computer Sciences, Physical Sciences and Earth Sciences, University of Messina, Via F. S. D'Alcontres 31, 98166, Messina, Italy

[25]Astrophysics Research Centre, School of Mathematics and Physics, Queen's University Belfast, BT7 1NN, UK

[26]Department of Astronomy, University of Cape Town, Private Bag X3, Rondebosch 7701, South Africa

[27]South African Astronomical Observatory, P.O. Box 9, Observatory 7935, South Africa

[28]Astrophysics Science Division, NASA Goddard Space Flight Center, Mail Code 661, Greenbelt, MD 20771, USA

Corresponding author: Jillian Rastinejad
jillianrastinejad2024@u.northwestern.edu

[29] *Clemson University, Department of Physics & Astronomy, Clemson, SC 29631 USA*

[30] *INAF-Osservatorio Astronomico di Capodimonte, Salita Moiariello 16, I-80131, Napoli, Italy*

[31] *DARK, Niels Bohr Institute, University of Copenhagen, Jagtvej 155, 2200 Copenhagen N, Denmark*

[32] *Department of Astronomy and Astrophysics, California Institute of Technology, Pasadena, CA 91125, USA*

[33] *Center for Astrophysics and Cosmology, Science Institute, University of Iceland, Dunhagi 5, 107 Reykjavik, Iceland*

[34] *Institute of Astronomy, National Tsing Hua University, Hsinchu 30013, Taiwan*

[35] *Department of Physics & Astronomy, University of Utah, Salt Lake City, UT 84112, USA*

[36] *University of Hawaii Institute for Astronomy, 34 Ohia Ku Street, Makawao, HI 96768, USA*

[37] *Institute for Astronomy, University of Hawai'i at Manoa, 2680 Woodlawn Drive, Honolulu, HI 96822, USA*

[38] *INAF–Osservatorio di Astrofisica e Scienza dello Spazio, via Piero Gobetti 93/3, I-40129 Bologna, Italy*

[39] *School of Physics and Centre for Space Research, University College Dublin, Belfield, Dublin 4, Ireland*

[40] *Department of Astronomy and Astrophysics, University of California, 1156 High Street, Santa Cruz, CA 95064, USA*

[41] *University of California Observatories, 1156 High Street, Santa Cruz, CA 95064, USA*

[42] *Instituto de Astrofísica de Canarias, E-38205 La Laguna, Tenerife, Spain*

[43] *Departamento de Astrofísica, Univ. de La Laguna, E-38206 La Laguna, Tenerife, Spain*

[44] *School of Physics and Astronomy, Sir William Henry Bragg Building, Woodhouse Ln., University of Leeds, Leeds LS2 9JT, UK*

[45] *Department of Physics, Lancaster University, Lancaster, LA1 4YB, UK*

[46] *Université Paris-Saclay, Université Paris Cité, CEA, CNRS, AIM, 91191 Gif-sur-Yvette, France*

[47] *INAF–Osservatorio Astronomico di Roma, via Frascati 33, I-00040 Monte Porzio Catone, Italy*

[48] *Astronomical Institute Anton Pannekoek, University of Amsterdam, 1090 GE Amsterdam, The Netherlands*

[49] *Anton Pannekoek Institute for Astronomy, University of Amsterdam, 1090 GE Amsterdam, The Netherlands*

[50] *INAF—Istituto di Astrofisica Spaziale e Fisica Cosmica di Milano, Via A. Corti 12, 20133 Milano, Italy*

[51] *Aix Marseille University, CNRS, CNES, LAM, Marseille, France*

[52] *Institute for Gravitational Wave Astronomy, Henan Academy of Sciences, Zhengzhou 450046, Henan, China*

ABSTRACT

With a small sample of fast X-ray transients (FXTs) with multi-wavelength counterparts discovered to date, their progenitors and connections to γ-ray bursts (GRBs) and supernovae (SNe) remain ambiguous. Here, we present photometric and spectroscopic observations of SN 2025kg, the SN counterpart to the FXT EP 250108a. At $z = 0.17641$, this is the closest known SN discovered following an *Einstein Probe* (*EP*) FXT. We show that SN 2025kg's optical spectra reveal the hallmark features of a broad-lined Type Ic SN. Its light curve evolution and expansion velocities are comparable to those of GRB-SNe, including SN 1998bw, and two past FXT SNe. We present JWST/NIRSpec spectroscopy taken around SN 2025kg's maximum light, and find weak absorption due to He I $\lambda1.0830, \lambda2.0581$ μm and a broad, unidentified emission feature at ~ 4–4.5 μm. Further, we observe broadened Hα in optical data at 42.5 days that is not detected at other epochs, indicating interaction with H-rich material. From its light curve, we derive a ^{56}Ni mass of 0.2 - 0.6 $M_\odot$. Together with our companion paper (Eyles-Ferris et al. 2025), our broadband data are consistent with a trapped or low energy ($\lesssim 10^{51}$ ergs) jet-driven explosion from a collapsar with a zero-age main sequence mass of 15–30 $M_\odot$. Finally, we show that the sample of *EP* FXT SNe support past estimates that low-luminosity jets seen through FXTs are more common than successful (GRB) jets, and that similar FXT-like signatures are likely present in at least a few percent of the brightest Ic-BL SNe.

Keywords: Gamma-ray Bursts, Supernovae

1. INTRODUCTION

Though first discovered in the era of sounding rockets (e.g. Cooke 1976), and highlighted by discoveries with *Chandra* and *XMM-Newton* (Jonker et al. 2013; Alp & Larsson 2020; Quirola-Vásquez et al. 2023), the nature of fast X-ray transients ("FXTs"; non-repeating transients detected in the X-ray) and their connection to the deaths of massive stars and luminous, jetted γ-ray bursts (GRBs) remains uncertain. By definition, FXTs represent a broad category of transients. In some cases, FXTs could represent the tail of the emission from classical GRBs whose spectra peak at tens to hundreds of

keV. FXTs also encompass the population of so-called X-ray Flashes ("XRFs"; Heise et al. 2001; Sakamoto et al. 2005), a historical "sub-type" of GRBs defined by a greater ratio of fluence in the X-ray compared to the γ-ray bands. Most notably, this XRF/FXT group includes the nearby, serendipitous discoveries of Type Ib/c supernovae (SNe), SN 2006aj (Campana et al. 2006; Pian et al. 2006; Soderberg et al. 2006) identified in the long GRB/XRF 060218 and the X-ray-only discovery of the much less luminous SN 2008D (Soderberg et al. 2008). These discoveries showed that at least some FXTs are produced by the core-collapse of massive, stripped-envelope stars. Though sharing similarities with the broad-line Type Ic (Ic-BL) SNe accompanying GRBs (GRB-SNe), the SNe associated with XRFs demonstrate considerable diversity compared to GRB SNe. For example, two SNe (SN 2008D and SN 2010bh; Soderberg et al. 2008) following these XRFs were $\approx$ $5 - 100$ times less luminous compared to the prototypical GRB-SN, GRB 980425/SN 1998bw. Further, one (SN 2008D) showed absorption due to He (Soderberg et al. 2006; Modjaz et al. 2009), potentially representing a stage in the continuum of massive star explosions (e.g., Galama et al. 1998; Clocchiatti et al. 2011; Soderberg et al. 2008; Alp & Larsson 2020). However, with a limited sample of such events to date, the mapping of GRBs to FXTs, XRFs or core-collapse SNe without high-energy emission continues to be an open question.

Previously, the lack of a dedicated discovery mission meant that the FXT sample was limited to rare, serendipitous detections (e.g., Soderberg et al. 2006, 2008) or archival searches in narrow-field instruments such as *Chandra* or *XMM-Newton* (Jonker et al. 2013; Glennie et al. 2015; Bauer et al. 2017; Alp & Larsson 2020; Novara et al. 2020; Lin et al. 2022; Quirola-Vásquez et al. 2022, 2023). The small ($\lesssim$40) population size of FXTs and paucity of multi-wavelength counterparts resulted in large uncertainties on their rates, local environments, and counterpart properties. Uncertainties on these properties inhibit a full understanding of how FXTs fit within the landscape of transients. In particular, many events discovered in the narrow-field searches were of long duration (hundreds to thousands of seconds) compared to GRBs. At present, it is unclear if these long durations represent a selection effect or fundamentally different physical processes (e.g. Levan et al. 2024b). At the same time, the realization of substantial diversity in the progenitors of long GRBs, including events likely produced by compact object mergers (e.g. Rastinejad et al. 2022; Troja et al. 2022; Yang et al. 2022; Levan et al. 2024c), erases the assumption that FXTs arise exclusively via core-collapse.

The 2024 launch of a wide-field soft X-ray monitor onboard the *Einstein Probe* (*EP*), opened a new route to discover FXTs and characterize their multi-wavelength counterparts (Yuan et al. 2015, 2022). Critically, *EP* is able to detect FXTs with its Wide Field X-ray Telescope (WXT; 3600 sq. degree field of view), localize them via WXT to $\sim$ 3 arcminute precision, and subsequently re-point a narrow-field follow-up telescope to obtain $\sim$ 10 arcsecond position. As such, the latency of FXT announcements has reduced from days (and, often, year timescales) to minutes (e.g., Zhang et al. 2024; Li et al. 2025a). This speed increase offers the unprecedented ability to locate multi-wavelength counterparts and unveil their origins.

In its first year alone, *EP* discovered dozens of extragalactic FXTs, revealing a diversity of counterparts and environments. While several FXTs have been associated with GRBs (e.g., Yin et al. 2024; Frederiks et al. 2024; Liu et al. 2025), others have no observed prompt GRB counterpart despite constraints from γ-ray facilities, prompting speculation that their progenitors are distinct from GRBs produced following core-collapse (e.g., Sun et al. 2024; Bright et al. 2024; van Dalen et al. 2025; Busmann et al. 2025; O'Connor et al. 2025). At least four *EP* events are known to originate at redshifts $z > 3.5$ (Bochenek et al. 2024; Levan et al. 2024a,b; Liu et al. 2025), representing an exciting new path to exploring the distant Universe but limiting detailed studies of multi-wavelength counterparts. Notably, the counterpart of EP 240414a was localized to a galaxy at $z = 0.401$ and revealed the spectroscopic signatures of a Ic-BL SN. Critically, this event established that at least some *EP* FXTs originate from the explosions of massive stars (van Dalen et al. 2025; Sun et al. 2024). However, at this redshift, late-time spectroscopic and photometric follow-up of the SN was limited (Sun et al. 2024; van Dalen et al. 2025; Srivastav et al. 2025). More recently, the event EP 250207b was potentially associated with a galaxy at $z = 0.082$ (Levan et al. 2025a). However, at present, no evidence of an SN counterpart has been announced and published observational limits appear to rule out a SN (Yang et al. 2025).

On 8 January 2025 at 12:30:28.34 UT, *EP* discovered a new FXT, EP 250108a, with a duration of $\sim 960^{+3092}_{-208}$ s (Li et al. 2025a,b). Later analysis of *Fermi*-GBM observations place a conservative, sky-averaged upper limit on associated emission in the 10-1000 keV band of $f_\gamma < 2.6 \times 10^{-8}$ erg cm^{-2} s^{-1} at 415 s following the initial trigger (*Fermi*'s view of the localizaton was occulted by Earth prior to this time; Ravasio et al. 2025). Prompt follow-up observations were not taken, but imaging obtained $\sim$ 1.5 days after the outburst revealed a blue and

rapidly-fading counterpart with a redshift of $z = 0.17641$ (Eyles-Ferris et al. 2025). Beginning at ≈ 6 days following the initial trigger, the cooling, optical counterpart began to rise in brightness. Spectra taken by the Nordic Optical Telescope (NOT) and Gemini-North at $\delta t \sim 10$ days (where δt refers to the observer-frame time since the *EP* trigger) showed the signatures of a Ic-BL SN, dubbed SN 2025kg (see Section 2.2 for further analysis; Levan et al. 2025b; Xu et al. 2025; Srinivasaragavan et al. 2025). SN 2025kg offers a unique first opportunity for a detailed comparison between the multi-band light curves and spectroscopic properties of FXT SNe, GRB-SNe and stripped-envelope SNe observed without high-energy counterparts, shedding light on FXT progenitors.

Here, we present optical and infrared observations and analysis of SN 2025kg, including *James Webb Space Telescope* (JWST) spectroscopy. This work represents a companion paper to Eyles-Ferris et al. (2025) which contains an in-depth analysis of the early ($\lesssim 6$ days post-trigger) observations as well as analysis of the radio and high-energy data. In Section 2 we detail our extensive photometric and spectroscopic campaign to characterize SN 2025kg. In Section 3 we analyze our observations, highlight key features in the JWST spectrum, and compare the properties of SN 2025kg to those of past stripped envelope SNe associated with FXTs, GRBs and discovered without high-energy triggers. In Section 4 we describe our photometric modeling of SN 2025kg. In Section 5, we infer properties of the progenitor from our observations, including its zero-age main sequence (ZAMS) mass, constraints on a He shell due to common envelope mass ejection, and contextualize FXT SNe in the wider population of Ic-BL SNe. Throughout this work, we assume a Planck cosmology, (Planck Collaboration et al. 2020) report all magnitudes in the AB system, and assume an event redshift of $z = 0.17641 \pm 0.0003$ (Eyles-Ferris et al. 2025).

2. OBSERVATIONS

2.1. *Photometry*

Here, we present optical and near-infrared (IR) photometry of SN 2025kg covering $6 < \delta t < 66.5$ days (observed frame; observations at $\delta t \lesssim 6$ days are presented in Eyles-Ferris et al. 2025). We obtained optical observations with the Alhambra Faint Object Spectrograph and Camera (ALFOSC) on the NOT, the IO:O on the Liverpool Telescope (LT), the Gemini Multi-Object Spectrographs (GMOS) on the Gemini-North and South Telescopes, Pan-STARRS, BlackGEM (for *q*-band description see Groot et al. 2024), the Multi-Object Double-beam Spectrograph (MODS) on
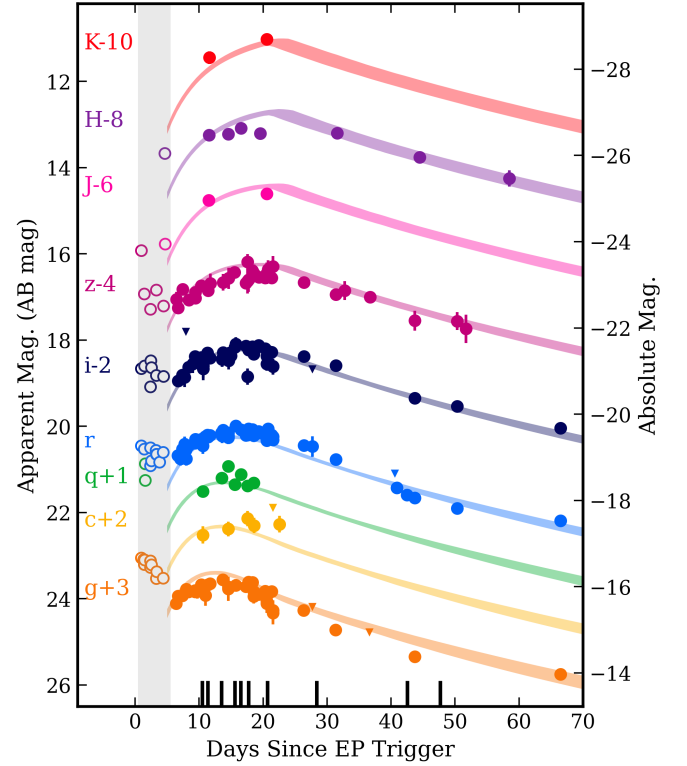

Figure 1. Optical-near-IR detections (circles) and upper limits (triangles) of the counterpart to EP 250108a. The data at $\delta t > 6$ days is well-described by a one-zone radioactive decay model (lines; Arnett 1982; Sarin et al. 2024) with an ^{56}Ni mass of $0.6 \pm 0.1 M_\odot$ (Section 4). Observation during the fast-cooling phase prior to the emergence of SN 2025kg ($\delta t < 6$ days; open symbols and grey vertical band) are discussed in detail in Eyles-Ferris et al. (2025). We also show the times of the spectroscopic observations with black vertical lines at the bottom of the figure.

the Large Binocular Telescope (LBT), the Goodman spectrograph on the Southern Astrophysical Research (SOAR) Telescope, the Lulin Observatory, MegaCam on the Canada-France-Hawaii Telescope (CFHT), and T80S-Cam on T80S. All optical images were processed using standard techniques, including Gemini DRAG-ONS (Labrie et al. 2019), a custom python pipeline, POTPyRI[1], `photpipe` (see Rest et al. 2005; Santos et al. 2024, for details), a dedicated LBT data reduction pipeline (Fontana et al. 2014), a modified version of the `photometry-sans-frustration` package `psf` (Nicholl et al. 2023), the `Elixir` pipeline (Magnier & Cuillandre 2004), a custom built pipeline[2], as well as a combination of standard `PyRAF` tasks (Science Software Branch

---

at STScI 2012) and the `LACosmic` task (van Dokkum 2001).

We obtain photometry directly on each image using a common set of standard stars drawn from Pan-STARRS (Flewelling et al. 2020). We do not anticipate significant ($\gtrsim$ 0.6 mag) contamination from the underlying host galaxy given its faintness relative to the transient as measured in archival Legacy Survey imaging (g = 23.40 ± 0.04 mag, r = 23.13 ± 0.02 mag, i = 22.99 ± 0.06 mag, z = 22.89 ± 0.08 mag; Dey et al. 2019). In addition, we obtained near-IR imaging with FLAMINGOS2 on Gemini-South and the MMT and Magellan Infrared Spectrograph (MMIRS) on the MMT. We process all near-IR images using DRAGONS and POTPyRI and obtain photometry using a common set of standard stars from the Two Micron All Sky Survey (2MASS; Skrutskie et al. 2006).

We provide details for all photometric programs in Appendix Table 2. We further incorporate detections from the GCNs (Ror et al. 2025; Song et al. 2025; Zou et al. 2025) and ATLAS forced photometry (co-bands; Tonry et al. 2018). We present all photometry in AB magnitudes in Appendix Table 3 and show our observations in Figure 1.

2.2. Spectroscopy

We present thirteen optical spectra of SN 2025kg taken over $\delta t = 10.5 - 47.7$ days. Spectroscopy prior to the emergence of SN features ($2.6 < \delta t < 4.6$ days) is presented and analyzed in our companion paper (Eyles-Ferris et al. 2025). Our optical spectroscopy was obtained with GMOS on the Gemini-North and South Telescopes (Program IDs GN-2024B-Q-107, GN-2024B-Q-131, GS-2024B-Q-105, GS-2025A-Q-107, P.I.s Rastinejad, Huber), OSIRIS+ on the Gran Telescopio Canarias (Program ID GTC1-24ITP; P.I. Jonker), the Multi Unit Spectroscopic Explorer (MUSE) on the Very Large Telescope (VLT; Program ID 111.259Q.001, P.I. Jonker), and the Low Resolution Imaging Spectrometer (LRIS) on Keck Observatory (P.I.s Harrison, Prochaska). Details of each spectroscopic set up are logged in Appendix Table 4.

We reduce Keck and Gemini spectroscopy using `PypeIt` (Prochaska et al. 2020). To account for instrumental flexure, sub-pixel shifts in the position of the [O I] 6300 Å sky emission line were measured and applied as corrections. We reduce GTC spectra using `Molly` to correct for the Earth's motion relative to the target and observations of spectrophotometric standard stars taken the same night for flux calibration. We reduce the VLT spectrum using ESO-reflex (Freudling et al. 2013). We process the LBT spectrum using the Spectroscopic In-
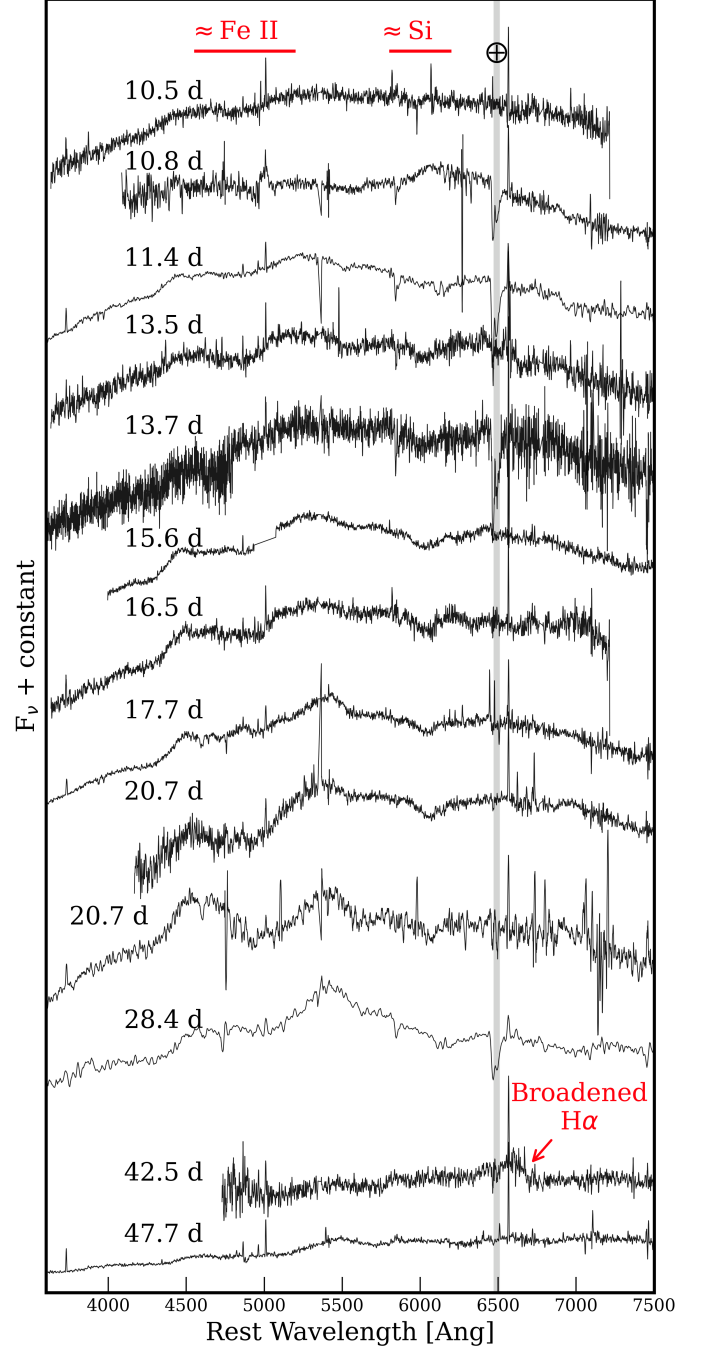

Figure 2. Our spectroscopic sequence of SN 2025kg. We observe broad absorption features around ∼5000 Å and ∼6100 Å that we ascribe to Fe II λ5169 and Si λ6355. In the spectrum at $\delta t = 42.5$ days we observe broadened Hα emission. We mark the location of a telluric feature with a ⊕.

teractive Pipeline and Graphical Interface (SIPGI) tool (Gargiulo et al. 2022) and perform wavelength calibration using arc lamp frames. To obtain flux-calibrated LBT spectrum, we applied the sensitivity function derived from the spectro-photometric standard star Feige
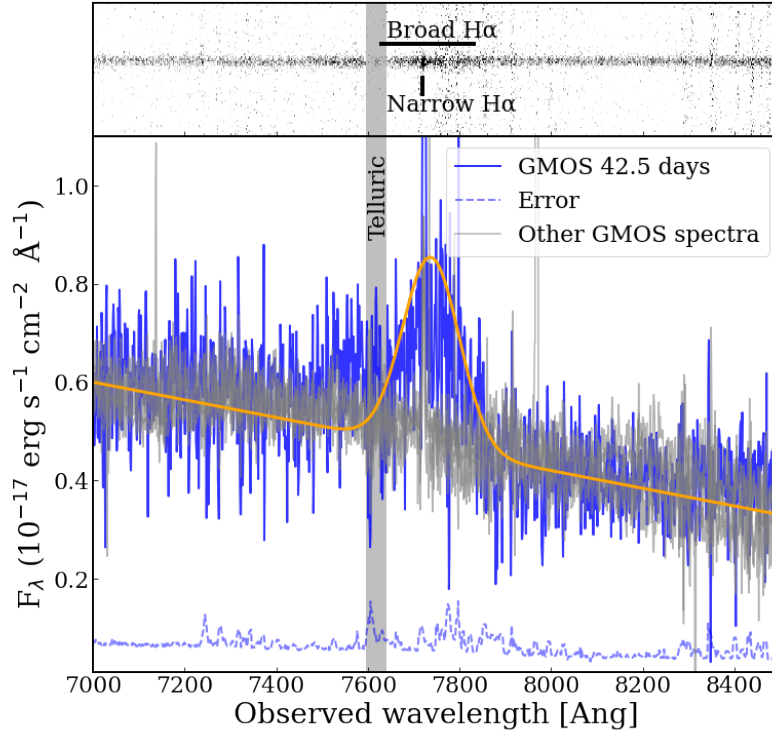
Figure 3. Images of the 2D (top) and 1D (bottom) GMOS spectrum of SN 2025kg taken at $\delta t = 42.5$ days, centered around Hα $\lambda6562.8$ Å. For comparison, we show our other GMOS spectra in grey, which show only the narrow Hα component. In addition to the narrow component, which is present in other epochs (Figure 2) and likely due to the underlying host galaxy, we observe broad, underlying emission, indicating an H-rich source is interacting with SN 2025kg at this epoch. We show an orange Gaussian superimposed on the continuum for visual purposes.

34. We correct all spectra for Galactic extinction in the direction of the burst ($A_V = 0.049$ mag; Schlafly & Finkbeiner 2011) and show the optical spectroscopic series in Figure 2.

In each spectrum, we identify the distinct signatures of Type Ic-BL SNe. For instance, we observe at least two broad absorption features around the expected locations of Fe II $\lambda5169$ (or a blend of the Fe triplet) and Si $\lambda6355$ (Figure 2) and no prominent absorption around the optical features of H or He. In several of the spectra we observe narrow emission lines, including those at the rest-frame locations of Hα, Hβ, and [OIII]$\lambda4958, 5007$, which we attribute to the underlying host galaxy. To compare SN 2025kg to other SNe, we utilize the spectral template matching tool, `gelato` (Harutyunyan et al. 2008), which matches an input spectrum to a large bank of observed SNe spectra at a range of phases. For the SN 2025kg spectrum observed at $\delta t = 17.7$ days `gelato` finds a strong match to the Type Ic-BL SN 2006aj (associated with GRB/XRF 060218) at 0.8 days past peak provides the strongest fit. For the SN 2025kg spectrum observed at $\delta t = 28.4$ days, `gelato` finds strong matches to sev-

eral Type Ic-BL SNe, including SNe 1997ef, 1998bw, 2002ap and 2006aj. This analysis definitively confirms our classification of SN 2025kg as a Type Ic-BL SN.

In the GMOS spectrum at $\delta t = 42.5$ days (Figure 3) we observe a broadened Hα emission feature, distinct from the narrow Hα emission observed in previous epochs (Figure 2). We inspected the individual four 2D spectral frames of the $\delta t = 42.5$ days spectrum and observe evidence for excess emission associated with this broadened feature in each. We do not see significant broadened Hα emission in the previous ($\delta t = 28.4$ days) or subsequent ($\delta t = 47.7$ day) spectra. We discuss this feature in greater detail in Section 3.2.

In addition, we obtained two near-IR spectra of SN 2025kg. At $\delta t = 12.7$ days post-burst we obtained a cross-dispersed spectrum covering $0.82 - 2.5$ μm with the Gemini Near-InfraRed Spectrograph (GNIRS) on Gemini-North (Program ID GN-2024B-Q-107, P.I. Rastinejad). These data were processed in `Pypeit` with additional post-processing performed following methods described in Tinyanont et al. (2024). Due to low signal-to-noise over the majority of the
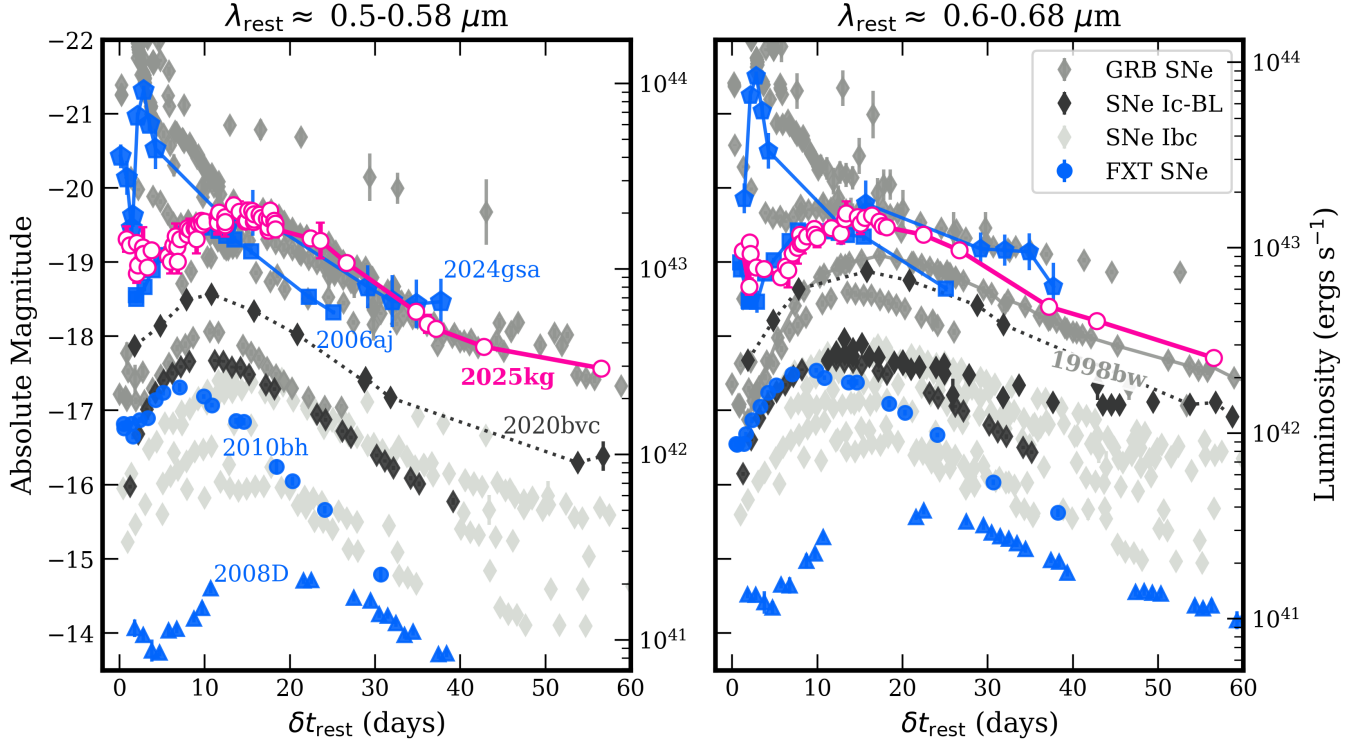
Figure 4. Light curve comparison of SN 2025kg (pink circles) and SNe associated with FXTs (blue), GRB-SNe (grey diamonds), SNe Ic-BL observed without GRB counterparts (dark grey diamonds), and SNe Ib/c (light grey diamonds). Observations are corrected for Milky Way extinction (Schlafly & Finkbeiner 2011) and presented in the nearest rest-frame band using the event's known redshift. The light curve of SN 2025kg strongly resembles those of SN 1998bw, SN 2006aj and SN 2024gsa in its peak luminosity and temporal evolution.

bandpass, we consider only the portion $\lesssim 1.25$ μm usable. Further, at $\delta t = 17.2$ days, we obtained fixed slit spectroscopy with NIRSpec on JWST (Program 6133; P.I. Gompertz) using the prism (covering 0.5-5 microns) at low resolution, and with an exposure time of 6302 seconds. At the time of the JWST spectroscopy the source is point-like and several magnitudes brighter than the anticipated magnitude of its compact underlying host galaxy. Therefore, we utilize the default pipeline reduction and 1D extraction of the NIRSpec observations.

3. ANALYSIS & COMPARISON TO PAST EVENTS

3.1. *SN Light Curves*

To place SN 2025kg in context of past GRB-SNe, FXT-SNe, and other stripped-envelope SNe, we compare its light curve to those of relevant past events. We include eleven events with X-ray or GRB counterparts: SN 1998bw (GRB 980425; Clocchiatti et al. 2011), SN 2003dh (GRB 030329; Matheson et al. 2003), SN 2006aj (GRB/XRF 060218; Mirabal et al. 2006; Soderberg et al. 2006), SN 2008D (XRF 080109; Soderberg et al. 2008) SN 2010bh (GRB/XRF 100316D; Cano et al. 2011; Olivares E. et al. 2012), SN 2011kl (GRB 111209A; Levan et al. 2014;

Greiner et al. 2015) SN 2013cq (GRB 130427A; Perley et al. 2014), SN 2016jca (GRB 161219B; Cano et al. 2017), SN 2017iuk (GRB 171205A; Izzo et al. 2019), SN 2019oyw (GRB 190829A; Hu et al. 2021; Rastinejad et al. 2024), and SN 2024gsa (EP 240414a; Srivastav et al. 2025). For events without high-energy counterparts, we show a subset of Type Ib/c and Ic-BL SNe from the literature (Foley et al. 2003; Drout et al. 2011; Izzo et al. 2020; Ho et al. 2020), which we normalize in time to the peak of SN 2025kg in each respective filter. We show all light curves in the nearest rest-frame filter using their known redshifts (Figure 4).

This comparison (Figure 4) highlights that SN 2025kg's luminosity is comparable to most GRB-SNe, particularly SN 1998bw, and distinct from SNe observed without high-energy counterparts. Amongst the SNe associated with FXTs, the closest analogs of SN 2025kg are SN 2006aj and SN 2024gsa, the latter of which is also associated with an *EP* FXT. The optical light curve of SN 2024gsa is marked with a large flare between $\delta t = 1.5 - 3$ days (e.g., Srivastav et al. 2025; van Dalen et al. 2025), which we do not observe in early observations of SN 2025kg (Eyles-Ferris et al. 2025).
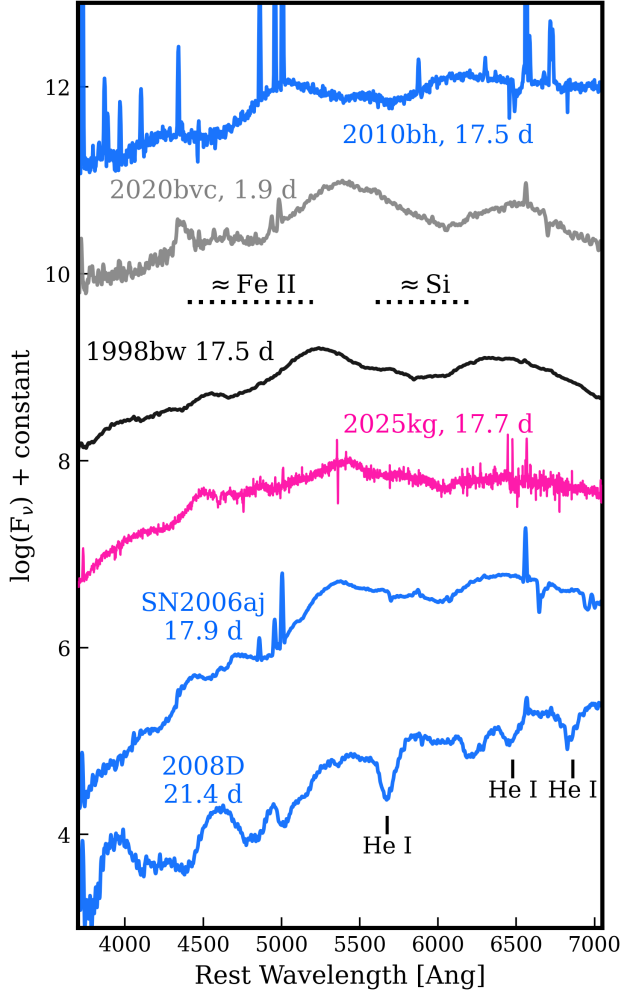
Figure 5. Comparison of SN 2025kg spectra (pink) to SN 1998bw (black; Patat et al. 2001), and three SNe associated with FXTs (blue), SN 2006aj (Pian et al. 2006), SN 2008D (Modjaz et al. 2009, 2014) and SN 2010bh (Bufano et al. 2012) around their SNe peak. We also show a spectrum of the Ic-BL SN 2020bvc (Hiramatsu et al. 2020) taken ∼1.9 days post-explosion. We label the approximate locations of Fe II λ5169 Åand Si λ6355 Å. Due to its broad-lined features and lack of He lines (labeled in SN 2008D) SN 2025kg is comparable to SN 1998bw and SN 2006aj.

3.2. *SN 2025kg Spectra & Broadened Hα at δt = 42.5 days*

We next attempt to compare our spectra of SN 2025kg to past GRB-SNe, FXT SNe, Ic-BL SNe without a high-energy trigger, and AT 2018cow, the latter of which is a benchmark event showing broadened Hα emission (Prentice et al. 2018; Margutti et al. 2019; Perley et al. 2019). We download spectra from WISeREP (Yaron & Gal-Yam 2012) of the prototypical GRB-SN, SN 1998bw (Patat et al. 2001), three SNe associated with FXTs, SN 2006aj (Pian et al. 2006), SN 2008D

(Modjaz et al. 2006, 2014) and SN 2010bh (Bufano et al. 2012) and SN 2020bvc (Hiramatsu et al. 2020). Further, we incorporate spectra of the luminous fast blue optical transient, AT 2018cow, in which broadened Hα was prominently observed starting at ≈15 days following the event's detection (e.g., Margutti et al. 2019; Perley et al. 2019; Xiang et al. 2021).

In Figure 5 we show the spectra for GRB-SNe and FXT SNe within a week of the SN peak ($\delta t = 17.5 - 21.4$ days) and the spectrum of SN 2020bvc taken 1.9 days after the explosion (no later spectra are available on WISEReP). Spectra of the Type Ib SN 2008D show prominent He I λ 4471, 5876, 6678, 7061 Å absorption lines (Modjaz et al. 2009), which we do not observe in SN 2025kg. Considering the remaining spectra, at both epochs, SN 2010bh is less visually comparable to SN 2025kg than SN 2006aj and SN 1998bw, which we attribute in part to its larger ejecta velocities (see Section 3.3; Chornock et al. 2010). Similar to their light curve properties (Section 3.1) SN 1998bw and SN 2006aj are spectroscopically comparable objects to SN 2025kg (Section 2.2). SN 2020bvc also shows a comparable shape to SN 2025kg. We note that SN 2020bvc was also comparable to SN 2025kg in terms of photometric color, blackbody radius, and X-ray properties during the early ($\delta t \lesssim 6$ days) fast-cooling phase, as shown in our companion paper (Eyles-Ferris et al. 2025).

Turning to the broadened Hα emission, we fit a simple Gaussian profile to the feature (omitting the narrow component using `curvefit`, finding a full width at half maximum value of ∼50 Å. We next compare our SN 2025kg spectrum at $\delta t = 42.5$ days to those of SN 1998bw, SN 2010bh and AT 2018cow at $\delta t = 42.5 - 48.6$ days in the region of Hα (Figure 6). Spectra of SN 2006aj beyond 20 days of the initial high-energy trigger are not available on WISeREP. Compared to the spectrum of SN 2025kg binned at a resolution of 40 Å, the broadened emission feature is stronger and more narrow in AT 2018cow and absent or very weak in SN 2010bh. Though a comparable bump in the spectrum of SN 1998bw is observed, we note that this likely due to two absorption features on either side of Hα. Further, in SN 1998bw the spectral shape in this region is is broadly consistent across several weeks of observations. In contrast, in SN 2025kg the continuum is fairly flat over ∼ 5700−6000 Åat most epochs, but exhibits broad Hα at one single epoch (Figure 3). Thus, we conclude that absorption features cannot explain the broadened emission feature in SN 2025kg, and that its most likely interpretation is that it arises from H interaction.

Whether this feature is common in FXT SNe but not GRB-SNe, or if SN 2025kg is an outlier amongst other

FXT SNe remains to be seen. Indeed, since the H appears only in one spectrum it may be a transient feature that could occur more frequently in other Ic-BL SNe but is often missed because it appears only at later times, and is only visible for a short period. One potential explanation for this feature in SN 2025kg is interaction with an extended H shell of circumstellar material (CSM), as was considered for AT 2018cow (Margutti et al. 2019; Perley et al. 2019). However, in AT 2018cow the broadened Hα signature was stronger compared to the continuum and persisted over several weeks, and was generally narrower, whereas in SN 2025kg the feature is weaker and absent in the spectrum at $\delta t = 47.7$ days (Figure 2). Alternatively, this could be a signature of a stellar companion, as is observed in a small (1-5%) fraction of Type Ia SNe (Maguire et al. 2016; Tucker et al. 2020). A larger sample of spectra at $\delta t \gtrsim 30$ days is critical to exploring the presence and temporal evolution of broadened Hα in future FXT SNe. We further discuss implications of this feature in Section 5.3.

3.3. Broad Line Velocity Measurements

We compute the ejecta expansion velocity using the Doppler shift of the absorption minima ascribed to Fe II λ5169 Åand Si λ6355 Å, which are well-characterized in GRB-SNe (e.g., Chornock et al. 2010; Bufano et al. 2012). For each spectrum, we fit the wavelength region around the absorption feature with a linear continuum and Gaussian profile using `scipy.curvefit`, and determine the velocity using the absorption minima's shift relative to the rest-frame wavelength. We show the results from our fitting over time and compare to values for several GRB-SNe and an SN Ic-BL (Chornock et al. 2010) in Figure 7.

We derive the velocity evolution for both Fe II λ5169 and Si λ6355. Though slight discrepancies between the velocities are present at several epochs, we note that measurements of expansion velocity using different lines are known to produce inconsistent values, in part due the locations of each elements within different layers of the ejecta (Modjaz et al. 2016; Finneran & Martin-Carrillo 2024). We next compare to the Si λ6355 velocities of SNe 1998bw, 2002ap, 2006aj and 2010bh (Chornock et al. 2010) and the only other confirmed *EP* SN, SN 2024gsa (EP 240124A; Sun et al. 2024; van Dalen et al. 2025), for which one measurement at $\delta t \approx 15$ days is available (Figure 7, bottom panel; Sun et al. 2024). At this epoch, the expansion velocities of SN 2025kg and SN 2024gsa are comparable. Compared to the wider sample of events, SN 2025kg appears most closely related to SN 2006aj, although the temporal coverage is not equivalent. SN 2025kg has larger measured veloc-
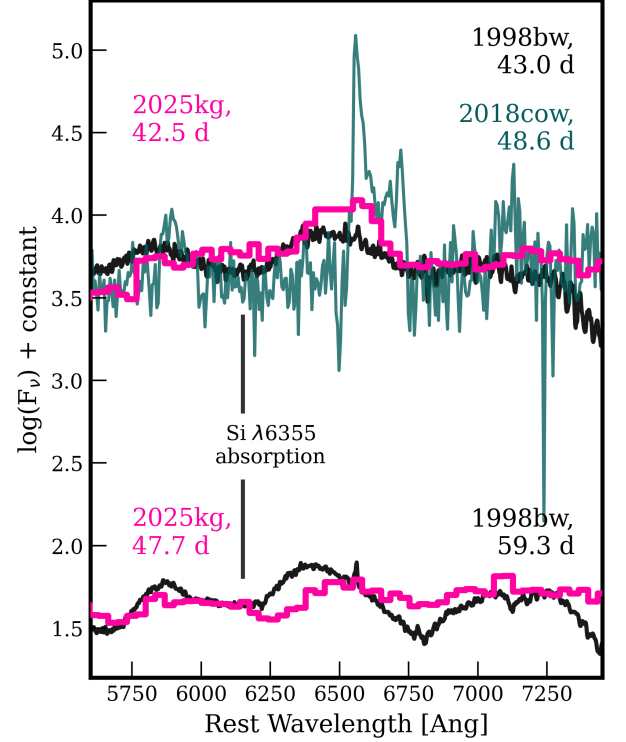
Figure 6. Spectra of SN 2025kg centered around Hα at $\delta t = 42.5$ and 47.7 days binned at 40 Å binned spectra (pink) in which regions affected by the telluric and narrow Hα have been removed. We observe a broadened Hα emission feature in the SN 2025kg Gemini-South/GMOS spectrum at $\delta t = 42.5$ days. We observe broadened Hα in the ESO/NTT spectrum of AT 2018cow (green) but not in the Danish/DFOSC spectrum of SN 1998bw (black) at similar epochs.

ities compared to the Ic-BL SN 2002ap and, generally, lower velocities compared to SN 1998bw and SN 2010bh.

3.4. Near-IR Evidence for Helium

Motivated by questions of the unknown stellar progenitors of FXTs, we next investigate to what degree He is present in the spectra of SN 2025kg. In our optical spectra, we do not observe prominent He I λ 4471, 5876, 6678, 7061 Å absorption lines, as were observed in SN 2008D (Figure 5; Soderberg et al. 2008). However, as He produces stronger signatures in the near-IR compared to the optical, we focus our search on the He I lines λ1.0830, λ2.0581 μm in the near-IR spectra. He I λ1.0830 is a prominent feature that dominates the 1 μm region in Type Ib SNe, and may be blended with C I λ1.0693 μm and Mg II λ1.0927 μm lines in Type Ic/Ic-BL SNe (e.g., Shahbandeh et al. 2022; Tinyanont et al. 2024). Though it is well-established that the He I λ1.0830 μm line is a more dominant line compared to He I λ2.0581 μm, the redder He I line has a greater off-
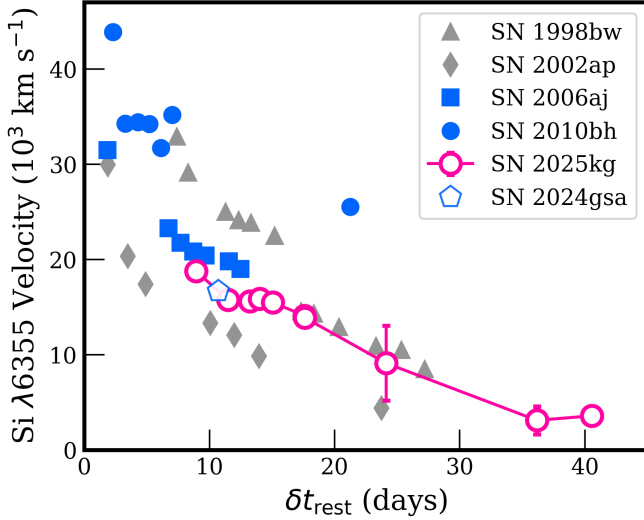
Figure 7. Si $\lambda 6355$ velocities of SN 2025kg (pink circles) along with literature values for GRB-SNe, FXT SNe and SNe Ic-BL 2002ap (Chornock et al. 2010). SN 2025kg comparable in absorption velocity to SNe 1998bw and 2006aj.

set from other potential absorption features and, thus, may be easier to distinguish as He I (Shahbandeh et al. 2022; Tinyanont et al. 2024). In the GNIRS spectrum, we do not observe any significant absorption features in the 1 μm regime, though we note that the majority of the spectrum has a low signal-to-noise.

Turning to the JWST spectrum, we observe a prominent, broadened absorption feature ~ 1 μm and, potentially, a shallower absorption feature ~ 2 μm (Figure 8). To investigate the source and significance of these features, we utilize a Bayesian toolkit to jointly model the 1 and 2 μm features as blended absorption features from multiple species with Gaussian components (Liu et al. 2023)[3]. We give the priors for our fits in Appendix Section 6.2. We note that the errors on velocity found through this method do not encompass uncertainties in the fit to the continuum. Thus, the true uncertainties are likely larger than those reported here.

First, we test the significance of the possible feature at ~ 2 μm as, if real, the feature would provide a second observational constraint on the presence of He I. We apply two models and compare their χ^2 and their Bayesian Information Criterion (BIC). The first model fits the 2 μm region with a linear function, a reasonable approximation for the continuum in the limited wavelength regime, while the second applies a Gaussian to represent an absorption feature. We find that the Gaussian model results in an improvement in χ^2 and BIC

[3] https://github.com/slowdivePTG/BayeSpecFit

~ 3500 compared to the linear fit, suggesting that the 2 μm feature is real.

We next evaluate fits to the 1 and 2 μ features for He I, C I and/or Mg II. The larger width of the 1 μm feature relative to the 2 μm feature (Figure 9) suggests a larger dispersion velocity. In turn, this implies that the 1 μm feature is not due to one element alone and is instead likely a blend of He I, C I and/or Mg II. Thus, we first fit both features for He I $\lambda 1.0830, \lambda 2.0581$ μm and C I $\lambda 1.0693, \lambda 2.1259$ μm (Figure 9). This fit finds He dominates the 2 μm feature and is blended with C I in the 1 μm feature. Both the C I ($17{,}600 \pm 200$ km s^{-1}) and He I ($14{,}500 \pm 100$ km s^{-1}) expansion velocities are similar to the Si velocities at a similar epoch (Figure 7). A second fit replacing C I with Mg II results in a similar He I velocity and a higher Mg II velocity ($21{,}700 \pm 100$ km s^{-1}). Finally, we explore if the 1 and 2 μm features can be explained with only C I and Mg II or a combination of the two (i.e., no He I). We find expansion velocities in the range of 24,000 - 41,000 km s^{-1}, $\approx 10{,}000$ km s^{-1} faster than the Si expansion velocities at a similar epoch (Figure 7). This finding implies that the 1 and 2 μm features are most reasonably fit with the presence of He I.

The most consistent expansion velocities with optical lines (Section 3.3) are derived from fits to these regions that include some He I. We also note that the best-fit pseudo-equivalent width ratio EW(He I $\lambda 1.0830 \mu$m)/EW(He I $\lambda 2.0581 \mu$m) from our first fit is ≈ 1, in line with predictions for these components (Lucy 1991), also consistent with the presence of He. Blending of He I and another feature is supported by a higher-resolution near-IR spectrum of SN 1998bw spectrum showing two "sub-features" within the 1 μm feature (Figure 9).

We conclude that there is likely a small amount of He in the ejecta of SN 2025kg, though a precise estimate is outside the scope of the current work. Based on the absence of He I lines in the optical (Figures 2 and 5) we place a conservative upper limit on He in the ejecta of $M_{\rm He} \lesssim 0.5 M_{\odot}$ (see, e.g., models for SN Ib/c optical spectra in Dessart et al. 2020, which are independent of engine type). The extent of He mixing in the ejecta may significantly impact the observed signature (e.g., Dessart et al. 2020, 2024).

In Figure 9 we show the SN 2025kg JWST spectrum and a near-IR SN 1998bw spectrum (8 days post-peak; Patat et al. 2001) in velocity space relative to the He I and Mg II features. Both spectra show evidence for absorption around the 1 and 2 μm features, with the 1 μm feature being most prominent. Near-IR spectra of SN 1998bw were taken at 8, 33 and 51 days post-
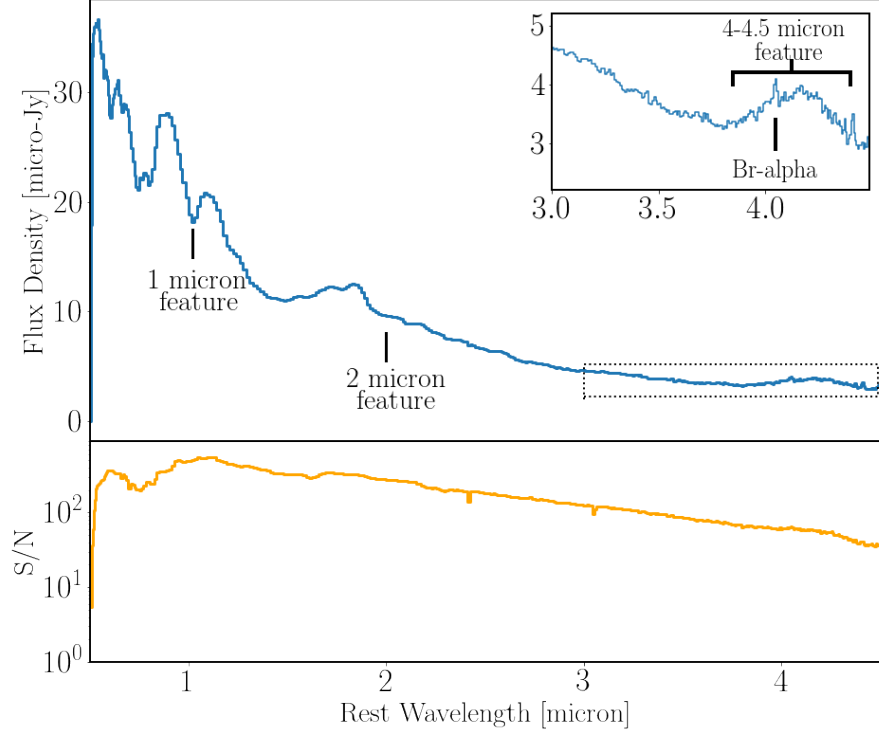
Figure 8. The JWST spectrum of SN 2025kg near maximum light. In the top and bottom panels we show the 1D spectrum and the signal-to-noise ratio (S/N), respectively. In the top panel, we highlight the three features discussed in detail in Section 3.4 (the 1 and 2 μm features) and Section 3.5 (the 4-4.5 μm feature, shown in the inset panel).

peak, and each shows a prominent feature near 1 μm ascribed to He I (Patat et al. 2001) which was not observed in a near-IR spectrum of SN 2010bh (Chornock et al. 2010). Further, in the SN 1998bw spectrum at +51 days post-peak Patat et al. (2001) also claim the detection of He I λ2.0581 μm and state this line is weakly detected in the spectra at +8 and +33 days post-peak (Patat et al. 2001). We observe a similar shape $\sim$ 2 μm in the spectra of SN 2025kg and SN 1998bw around peak (Figure 9). Altogether, this comparison demonstrates that small amounts of He are likely common in GRB-SNe and FXT SNe, but are not typically observed due to a paucity of near-IR spectroscopic coverage.

3.5. 4-4.5 μm Feature

We next turn to the broad emission feature centered at a rest-frame wavelength of $\sim 4.2\mu$m in JWST/NIRSpec spectrum taken around SN 2025kg's peak (Figure 8). Here, we discuss several potential explanations for this feature, but ultimately determine that a larger sample of observed events is critical to establishing its origin.

First, we investigate the possibility that this feature is a signature of r-process nucleosynthesis. Infrared excesses have been suggested as possible evidence of r-process, which may occur in the accretion disk after

the collapse of massive, rapidly-rotating stars, that are thought to be the progenitors of GRBs and some FXTs (e.g., Siegel et al. 2019; Zenati et al. 2020). To test this possibility, we explore if the 4.2 μm feature is consistent with a thermal signature. We find that this condition is not satisfied, as the feature is too narrow to be well fit with a Planck function. Further, the peak wavelength implies a temperature of $\sim$ 700 K, from which we infer a radius of $\sim 2 \times 10^{16}$ cm to match the luminosity. This would require an average expansion velocity of 0.9c over the first two rest-frame weeks, which is incompatible with both observations (Section 3.3) and theoretical expectations.

Second, we consider the possibility that this feature is due to dust. To investigate this, we consider comparable spectroscopic observations of SNe at mid-IR wavelengths to investigate their timescales for dust emergence, which are thus far limited in the literature. JWST NIRSpec and MIRI spectroscopic observations of the Type IIP SN 2022acko show no evidence for dust at 50 days following the explosion (Shahbandeh et al. 2024). In SN 1987A, near-IR spectra cover the range 1.05 μm – 4.1 μm (Meikle et al. 1989). The 4 μm region is dominated by a narrow emission feature that is attributed to Brackett α (λ_{peak} = 4.053 μm). H fea-
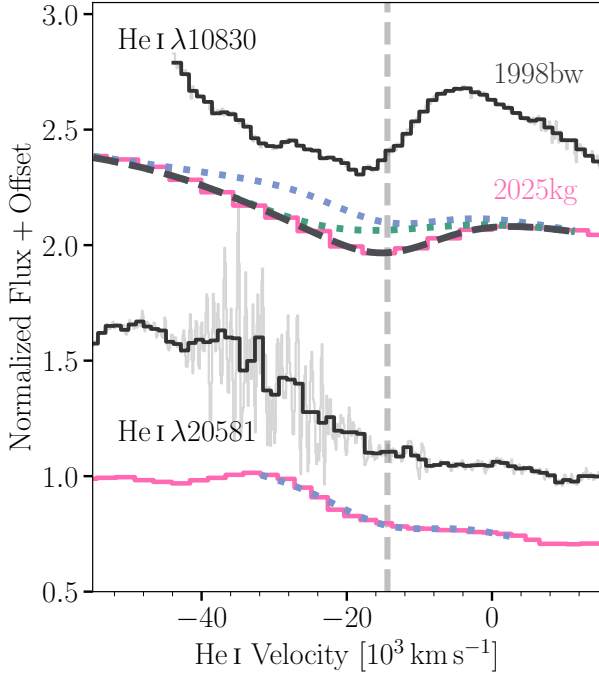
Figure 9. The JWST/NIRSpec spectrum of SN 2025kg
(pink) and the near-IR spectrum of SN 1998bw (black;
binned to mitigate telluric noise in the spectrum) in velocity
space $\sim$ the 1 μm (upper) and 2 μm (lower) features. We
show our combined fit (grey dashed) and individual contribu-
tions to the 1 μm feature due to C I (λ1.0693, λ2.1259 μm;
dotted turquoise) and He I (λ10830, λ20587; dotted blue)
absorption. We also mark the velocity derived from a single
Gaussian fit to the 1 μm feature with a vertical grey line.
In the top spectrum, the superposition of the C I and He I
absorption provides a strong fit to the observed feature. Our
analysis (Section 3.4) shows that a small ($\lesssim 0.5 M_\odot$) amount
of He is likely present in SN 2025kg.

tures are not expected in a Ic-BL SN like SN 2025kg,
although we note a narrow excess at this wavelength in
our spectrum (Figure 8), which may be emission from
the underlying host galaxy. In SN 1987A, at around
260 days post-peak a comparable broad underlying fea-
ture emerged and was tentatively suggested to be due
to an overtone of silicon monoxide (SiO) (Meikle et al.
1989). Both of these epochs are significantly later than
our JWST spectrum of SN 2025kg, which was taken at
$\approx$ 15 rest-frame days after the FXT trigger. Addition-
ally, at this point, the ejecta temperature is likely too
high for dust molecules to form, supporting that this
feature is not SiO. Further, spectral synthesis model-
ing indicates that the SiO overtone emission emerges at
$\gtrsim$ 100 days following core-collapse in Type Ic-BL SNe
(Liljegren et al. 2023).

Finally, the feature may be the result of nebular Fe
lines. This interpretation would require regions of the

ejecta to become optically thin, which may be possible
with high expansion velocities. Expansion velocities of
$\sim 0.1c$ were inferred at early time in Eyles-Ferris et al.
(2025), which may be sufficient to produce this signa-
ture. Looking forward, the assembly of a sample of mid-
IR spectra of stripped envelope SNe or other FXTs will
be important to understand how ubiquitous this feature
is, and shed light on its physical origin.

3.6. *Comparison of SN and High-Energy Properties*

In our companion paper, we show that
EP 250108a/SN 2025kg's prompt FXT, early ($\delta t \lesssim$
6 days) optical light curve, and radio upper limits are
consistent with a trapped or weak jet from a collapsar
(Eyles-Ferris et al. 2025). Motivated to explore if this
event is an typical FXT SN, we consider any potential
correlations between the high-energy and SN properties
of FXTs (Figure 10).

In addition to EP 250108a/SN 2025kg, we include the
events SNe 1998bw, 2006aj, 2008D, 2010bh, and 2024gsa
in this comparison. We utilize the prompt X-ray (2-
26 keV) emission of SN 1998bw detected by BeppoSAX
(Galama et al. 1998; Pian et al. 2000), X-ray detections
by *Swift*-XRT of SN 2006aj, SN 2008D, and SN 2010bh
pulled from UKSSDC (Evans et al. 2007, 2009), and the
prompt X-ray emission of SN 2024gsa and SN 2025kg ob-
served by *EP* (Sun et al. 2024; Li et al. 2025b). We
caution that these properties are drawn from a variety
of instruments, each with different energy ranges and
slewing strategies. However, we note that these compar-
isons span several orders of magnitude, mitigating some
biases. We mark the different instruments in Figure 10.
For SN properties, we incorporate SN peak magnitudes
derived from the light curves presented in Sections 3.1
and Si λ6355 velocities presented in Section 3.3.

Figure 10 highlights that SN 2025kg, SN 1998bw and
SN 2006aj occupy a similar region in the parameter
space of peak SN and peak X-ray luminosity (see also
Figure 13 of Eyles-Ferris et al. (2025)). We observe a
potential trend in these properties for the objects out-
side of this cluster, though a significantly larger sample
is needed to test this trend further. In terms of dura-
tion, the *Swift* events show a potential trend between
SN peak brightness and observed FXT duration. We
do not observe any correlations between the remaining
events.

4. RADIOACTIVE DECAY SN MODELING

With this extensive data set, we are motivated to con-
strain the physical properties of SN 2025kg, which en-
able comparisons to previous SN and possible proper-
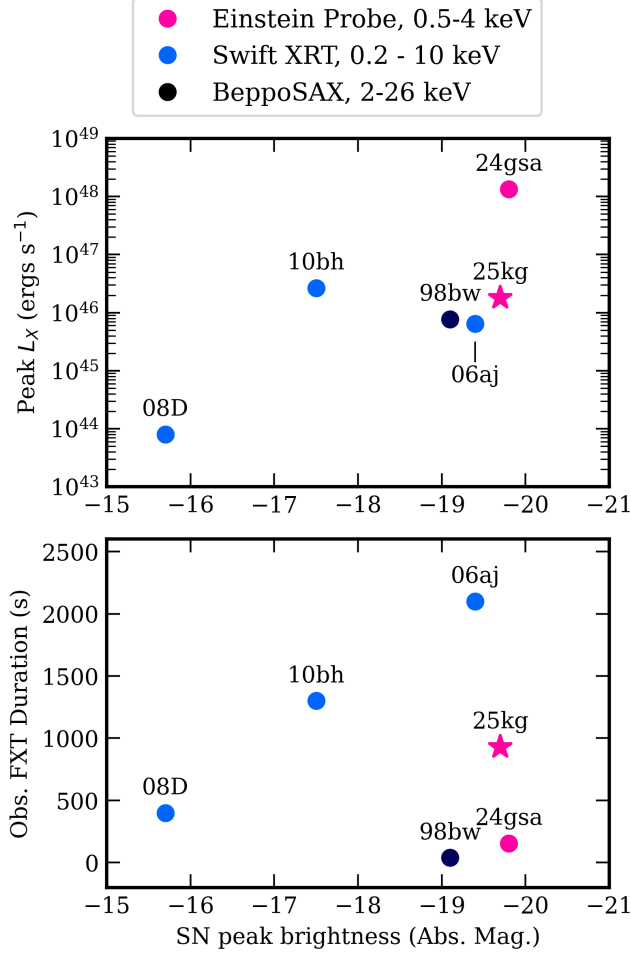ties of the progenitor. Thus, we fit the light curve for

Figure 10. Comparison of the SN peak time and FXT properties of several FXT events with SN counterparts (SNe 1998bw, 2006aj, 2008D, 2010bh, 2024gsa, 2025kg). EP 250108a/SN 2025kg is marked with a pink star in the first two rows. We caution that the different instruments' bandpasses and slewing strategies impact both the X-ray peak luminosities and durations, making direct comparisons inadvisable. However, the span of several orders of magnitude in some parameters mitigate some of these biases.

SN 2025kg using REDBACK (Sarin et al. 2024). We fit the light curve using two models: first, a one-zone "Arnett" model (Arnett 1982) and second, a model that accounts for mixing of ^{56}Ni into the outer ejecta.

For both models, we fit the entire light curve at $\delta t \gtrsim 6.5$ days assuming a Gaussian likelihood. For each photometric point, we include a systematic error of 0.15 mag added in quadrature to the statistical errors to capture any discrepancies caused by differences in photometric reduction, filter transmission curves, or in the model itself. We explore the model parameter space using Bayesian Inference via the PYMULTINEST

nested sampler (Buchner et al. 2014) through the BILBY library (Ashton et al. 2019).

4.1. One-zone Model

We begin with a one-zone "Arnett" model that assumes a one-zone, homologously-expanding ejecta powered by a centrally-located heating term (i.e., the ^{56}Ni) with a gray ejecta opacity that is constant in time. This model is commonly invoked to describe the physical properties of SNe. We consider 7 model parameters for the one-zone model here: ejecta mass, $M_{\rm ej}$; fraction of ^{56}Ni in the ejecta, $f_{\rm Ni}$; ejecta velocity, $v_{\rm ej}$; gray opacity, κ; γ-ray opacity, κ_γ; temperature at which the photosphere begins to recede, $T_{\rm floor}$; and host extinction in magnitudes, $A_{\rm v}$. For the final parameter, we assume a standard Fitzpatrick extinction law with an $R_v = 3.1$ (Fitzpatrick 1999). We use broad uninformative priors on each parameter.

Our model provides a strong fit to the data. Our fits with this model are shown in Figure 1 highlighting broad agreement with the data. We infer $1.4 \pm 0.15 M_\odot$ of ejecta with a ^{56}Ni mass of $0.6 \pm 0.1 M_\odot$ and an initial ejecta velocity of $19,000 \pm 700$ km s^{-1}. All uncertainties at 68% credible interval for the one-dimensional marginalized posterior. Our estimate of ejecta mass and energy is consistent with median values inferred from Type Ic-BL SNe (e.g., Taddia et al. 2019; Rodríguez et al. 2023; Srinivasaragavan et al. 2024) using a similar model. However, our estimate of the ^{56}Ni is marginally inconsistent with the Type Ic-BL SNe medial values of Taddia et al. (2019) (at 1σ), which could be due to differences in assumptions about γ-ray opacities or hinting towards a limitation with the one-zone model. We note that our analysis here is on the photometry, while past works have directly fit a reconstructed bolometric luminosity which could also explain the discrepancy.

4.2. Caveats to One-zone Model

There are clear limitations with one-zone model in its assumption of a centrally-located ^{56}Ni and constant opacity. In reality, the opacity is almost certainly not gray or constant with time (e.g., Niblett et al. 2025) and ^{56}Ni is likely mixed out to large radii due to Rayleigh-Taylor or jet-driven instabilities (e.g., Khatami & Kasen 2019; Reichert et al. 2023). The latter effect significantly impacts the overall bolometric light curve. In particular, the classical "Arnett-like" one-zone model often over-predicting the quantity of ^{56}Ni compared to models with mixing (e.g., Bersten et al. 2014) for two reasons. First, the central heating term is forced to overcome adiabatic losses compared to heating from ejecta at larger radii. Second, energy through heating has to diffuse

through more ejecta. Therefore, our ^{56}Ni mass measurement above is likely an overestimate. Additional luminosity in the form of a central engine could also provide an alternative path to powering the light curve which would naturally reduce the quantity of ^{56}Ni.

In Appendix Section 6.1 we present an alternate model in which ^{56}Ni is mixed with the outer SN layers, resulting in a lower best-fit value for the ^{56}Ni mass ($0.2\,M_\odot$). Though this model offers several advantages compared to the one described in Section 4, there are still uncertainties, such as the assumed mass profile, therefore, we conservatively use the ^{56}Ni estimate from both models. These masses and mixing provide some strong hints into the progenitor, as we discuss in Section 5.

Finally, we have assumed that the peak emission is powered entirely by ^{56}Ni decay. Shock heating can contribute to the peak emission, reducing the requirements on the ^{56}Ni mass (Niblett et al. 2025).

5. DISCUSSION

Our analysis of the light curves and spectra of SN 2025kg place strong constraints on the nature of the progenitor. In our companion paper (Eyles-Ferris et al. 2025) we argue that the engine behind this transient is jet-driven, supported by shock break-out model fits to the prompt X-ray emission, upper limits on radio emission and the blue and rapidly-fading light curve prior to the onset of the SN. In this section, we combine the inferences of both papers to discuss constraints on the progenitor and implications for the population of FXTs from collapsars.

5.1. Constraints on the ZAMS Mass of the Progenitor

Here, we determine the ZAMS mass of the progenitor by combining the inferred masses on the ejecta yield, the ^{56}Ni yield (which dictates the disk mass) and the compact remnant mass. We note that the ^{56}Ni mass may be overestimated due to luminosity contribution from additional sources, but do not anticipate this significantly impacts our order-of-magnitude estimates. To do this, we set the mass of the star at explosion to the C/O core mass as SN 2025kg shows evidence for stripping of its H and most of its He layers; Section 2.2. We assume that the C/O core mass will be equivalent to the summation of the ejecta mass, the disk mass and the compact object remnant mass. For the first component, we use the results from our light curve fits, which indicate a total ejecta mass of $0.8 - 1.4\,M_\odot$ with a ^{56}Ni mass of $0.2 - 0.6\,M_\odot$ in SN 2025kg (Section 4). We explore two scenarios to determine the latter two components: a black hole accretion disk jet model and a model invoking a neutron star accretion disk. If the remnant is

a black hole, we assume the accretion disk forms around a $3 - 5\,M_\odot$ black hole. If it is a neutron star, we assume an initial remnant mass of $1.4\,M_\odot$.

The large amount of ^{56}Ni ejecta mass required to explain the SN light curve peak (Section 4) indicates that a considerable mass must be processed through an accretion disk. In a jet-driven explosion, the ^{56}Ni is primarily produced in the high-temperature disk and ejected through a disk wind (Surman et al. 2006). Typically models predict that $\sim 20\%$ of the disk is lost through a wind (e.g Aktar et al. 2017; Siegel & Metzger 2017). This means that the mass that flows into the disk must be greater than 5 times that of the ^{56}Ni ejecta mass. To eject $0.2 - 0.6\,M_\odot$ of ^{56}Ni, roughly $1 - 3\,M_\odot$ would have to be processed through a disk. Combined with the non-nickel ejecta mass and the compact remnant mass, this corresponds to a C/O core of $\sim 3.0 - 5.2\,M_\odot$ for a neutron star accretion disk model or $\sim 4.6 - 8.8\,M_\odot$ for a black hole accretion disk model. Using the C/O star masses from low-metallicity stars simulated by (Woosley et al. 2002), the C/O core masses correspond to a ZAMS progenitor masses of $15 - 21\,M_\odot$ if the compact remnant is a neutron star and $19 - 30\,M_\odot$ if the compact remnant is a black hole. These mass ranges are consistent with our current expectations for the progenitors of neutron stars and black holes respectively (Fryer 1999). The uncertainty in the ^{56}Ni mass dominates the wide range of our predicted progenitor masses. A late-time observation of the light curve will help constrain the ^{56}Ni mass and place stronger constraints on the progenitor's ZAMS mass. Finally, we note that our above estimates are based on single star models with a fixed set of parameters for stellar evolution (e.g. mixing; Woosley et al. 2002). Models that include the effects of binary mass transfer and ejection are likely to alter or broaden the predicted range of progenitors. However, these results provide a first pass of the stellar conditions.

5.2. Constraints on a He Shell

In our companion paper (Eyles-Ferris et al. 2025) we find that the early optical light curve of the counterpart of EP 250108a ($\delta t \lesssim 6$ days) is marginally consistent with interaction of a $0.2 - 0.9\,M_\odot$ shell at a distance of 7×10^{14} cm. While we note that the preferred model to explain the early light curve is a shocked cocoon from a jet (Eyles-Ferris et al. 2025), here we briefly consider the implications of this alternate possibility for a shell around the progenitor of EP 250108a/SN 2025kg from our observations. This distance is consistent with being produced by a common envelope mass ejection of a He shell, and just below the lower radii predicted for He shell mass ejection from a common envelope if it occurs

at C ignition (Fryer et al. 2024). This distance is also consistent with a He merger event (Fryer & Woosley 1998; Grichener 2025).

Using the He shell models of Woosley et al. (2002) models, we predict a large amount of He in this shell ($> 1\,M_\odot$). This He shell will be swept up into the ejecta and behind the photosphere at the time of our optical spectra. Notably, this predicted shell mass is inconsistent with both the upper limit on the He mass of $< 0.5\,M_\odot$ from the optical spectra (Dessart et al. 2020; Section 3.4) and the mass of the shell derived in our companion paper (Eyles-Ferris et al. 2025). This He shell mass could be reduced if significant Wolf-Rayet mass loss occurs prior to the final mass ejection episode that produces the shell at 7×10^{14} cm. Alternatively, enhanced mixing (e.g. Frey et al. 2013) could reduce the size of the He shell. In conclusion, for our models to fit the data presented in Eyles-Ferris et al. (2025) and this work, either considerable wind mass-loss or stellar mixing is required.

5.3. *Implications of Hydrogen Observed at* $\delta t = 42.5$ *days*

In Section 2.2 we show that broadened Hα is observed at $\delta t = 42.5$ days, or when the shock reaches $\sim 10^{16}$ cm. Similarly, the Type I superluminous SN iPTF13ehe showed a similar late-time Hα feature initially observed in spectra at +251 days from peak light, which was interpreted as coming from a detached shell of H around 10^{16} cm from the progenitor star (Yan et al. 2017).

Here, we briefly consider several potential explanations for this feature. We find it unlikely that the H is due to the progenitor star's wind, as models robustly predict that a Wolf-Rayet wind would evacuate the H in a region with radial extent of 0.1-1 pc (Weaver et al. 1977).

One potential explanation could be that the Hα signature could be produced through interaction with a companion star. However, such a wide separation would argue that this companion star had no impact on the stellar evolution of the collapsing star. To ensure that the supernova blastwave sweeps up enough H to produce the Hα line, this companion would have to be evolved, either in a giant or supergiant phase (Hirai et al. 2018, 2020; Hirai 2023). Since we are likely to require a close binary to explain the rotation and loss of the He shell, this would then imply that the progenitor of SN 2025kg is in a triple system. However, we disfavor the triple companion explanation due the giant or supergiant phase requirement and the temporal likelihood of being in this phase. Furthermore, based on hydrodynamical simula-

tions, material stripped from a companion by the supernova ejecta will have velocities of order the escape velocity from the companion, too low to match the observed H broadening.

Alternatively, the Hα signature could be due to clumps of H-rich material surrounding the SN produced by an asymmetric common envelope mass ejection phase (e.g., Quataert et al. 2016; Fryer et al. 2020, 2023). These clumps could be sufficiently dense that they could persist despite the strong Wolf-Rayet wind (e.g., Owocki & Rybicki 1984; Puls et al. 2008). Post-SN binary interactions that cause ongoing energy injection through feedback from H-rich material accretion or through magnetar winds ablating an H-rich companion (E.g., Zhu et al. 2024) could produce a similar dense cloud. We favor this explanation for the Hα signature observed at $\delta t = 42.5$ days.

5.4. *A Growing Population of FXT-SNe & Connections to GRB-SNe and Ic-BL SNe*

Early works on XRF/FXTs with SNe found that the volumetric rates of such events would be at least an order of magnitude higher than those of collapsar GRBs (Soderberg et al. 2008). EP 250108a/SN 2025kg joins a population of three FXT-SNe (EP 240414a/SN 2024gsa, EP 250304a; van Dalen et al. 2025; Sun et al. 2024; Izzo et al. 2025) discovered in just the first year of *EP* operations. Of those with published SNe light curves and spectra (EP 240414a/SN 2024gsa and now EP 250108a/SN 2025kg) these events are comparable in their peak optical luminosities, optical spectra, and Si $\lambda6355$ Å absorption velocities (Sections 3.1-3.3) to GRB-SNe and the XRF/FXT 060218/SN 2006aj. Further, in Section 3.6, we demonstrated that the peak X-ray luminosities of GRB 980425, XRF/FXT 060218, and EP 250108a are also comparable. Taken together, these support a causal link between the progenitors and mechanisms driving GRBs and FXTs with SNe.

The three recent *EP* FXT detections and the rates of GRB-SNe discovered over the last 20 years ($\lesssim$1 per year; e.g., Dainotti et al. 2022) support earlier calculations (Soderberg et al. 2008) that FXT are significantly more common than GRB-SNe. While a robust calculation of the relative rates of FXT SNe and GRB-SNe is outside the scope of this work, we note that the three FXT SNe discovered in the first year of *EP* operations were at $z = 0.40, 0.17$ and 0.20 and detected by an instrument covering $\sim 9\%$ of the sky. From this, we derive an estimate of the intrinsic volumetric rates of at least several tens Gpc^{-3} yr^{-1}, 1-2 orders of magnitude larger than the rate of on-axis luminous GRBs (Sun et al. 2015).

In our companion paper, Eyles-Ferris et al. (2025) we demonstrate that EP 250108a/SN 2025kg is consistent with being driven by a collapsar-powered jet that either fails to break out of the dense circumstellar material or has an energy weaker than $\sim 10^{50} - 10^{51}$ ergs. Taken together with the rates, this indicates that trapped or weak jets are more common than the successful jets that produce GRBs. The lack of radio and X-ray detections at later times following EP 250108a/SN 2025kg (Eyles-Ferris et al. 2025) implies that observing any relativistic material may be challenging from these FXT-producing jets, in keeping with late-time radio surveys of Ic-BL SNe observed without high-energy counterparts (e.g., Corsi et al. 2016). Zooming out, it is likely that FXT-producing, "trapped" jets accompany a substantially larger fraction of Ic-BL SNe than those with successful jets and GRBs, representing at least a few percent of the Ic-BL SNe population.

Finally, we note that the SNe of two past FXT events, SN 2008D and SN 2010bh, are ∼5-100 times less luminous than FXT SNe 2006aj, 2024gsa, and 2025kg, and GRB-SNe and, in the former's case, show prominent He absorption (Figure 5; Soderberg et al. 2008; Modjaz et al. 2009). The lower optical luminosities of these SNe are echoed in the lower peak X-ray luminosities of their FXTs (Figure 10). Future *EP* detections of FXT SNe will reveal both the rates of such events and the full span in stellar progenitors of FXT SNe.

6. CONCLUSION

Along with our companion paper (Eyles-Ferris et al. 2025), we have presented the most detailed dataset to date of an SN accompanying an *EP* FXT. Our main conclusions are as follows:

- Optical spectra of SN 2025kg are characterized by broad absorption features due to Fe II $\lambda 5169$ and Si $\lambda 6355$ and do not show obvious emission due to He I, leading to a Type Ic-BL classification.

- SN 2025kg is a close analog of GRB-SNe, particularly SN 1998bw, and the FXT SNe, SN 2006aj and SN 2024gsa, in terms of its peak luminosity, expansion velocities, and spectral evolution. We also find a strong match between SN 2025kg and the Ic-BL SN 2020bvc, in keeping with comparisons to the early light curve (Eyles-Ferris et al. 2025).

- We observe absorption features ∼1 and 2 μm features in the JWST spectrum taken around maximum light, and find that they are well-fit with a combination of He I and C I. From optical spectra,

we conservatively conclude that the mass of He in the ejecta is $\lesssim 0.5 M_\odot$.

- We observe a broad feature at 4-4.5 μm in the JWST spectrum. We investigate several explanations for this feature, including thermal emission due to *r*-process nucleosynthesis, nebular Fe lines, and He emission, but cannot definitively identify its origin with present information.

- We fit SN 2025kg with a one-zone radioactive decay model and a model that accounts for mixing of ^{56}Ni into the outer SN ejecta. We derive a range in the ^{56}Ni mass of $0.2 - 0.6 \, M_\odot$.

- Together, observations presented in our companion paper (Eyles-Ferris et al. 2025) and this work favor a ZAMS progenitor mass for EP 250108a/SN 2025kg of $15-21 \, M_\odot$ or $21-30 \, M_\odot$ if the compact remnant is a neutron star or black hole, respectively. It is plausible that the progenitor was surrounded by a He shell ejected during a common envelope episode, and either H-rich clumps due to an prior, asymmetric common envelope ejection or a giant/supergiant tertiary stellar companion.

- Our analysis supports a causal link between GRB-SNe and FXT SNe, in which GRBs are produced by successful jets and FXT SNe are produced by trapped or weak jets. Thus far, the rate of SN detections following *EP* FXTs indicates that trapped or weak jets are substantially more common than successful (GRB) jets.

EP 250108a is only the second *EP* transient with an observed SN counterpart to date. Our detailed observational study of SN 2025kg has revealed both similarities with previous FXT and GRB SNe, and unexpected signals, including H at 42.5 days and the broad 4-4.5μm feature, that cannot be fully accounted for with current models. Looking forward, the opportunities for detailed observational studies to shed light on the stellar progenitors of FXTs and their catastrophic explosions is only increasing with the continued operations of *EP* and coordinated rapid follow-up efforts.

REFERENCES

Aktar, R., Das, S., Nandi, A., & Sreehari, H. 2017, MNRAS, 471, 4806, doi: 10.1093/mnras/stx1893

Alp, D., & Larsson, J. 2020, ApJ, 896, 39, doi: 10.3847/1538-4357/ab91ba

Arnett, W. D. 1982, ApJ, 253, 785, doi: 10.1086/159681

Ashton, G., Hübner, M., Lasky, P. D., et al. 2019, ApJS, 241, 27, doi: 10.3847/1538-4365/ab06fc

Bauer, F. E., Treister, E., Schawinski, K., et al. 2017, MNRAS, 467, 4841, doi: 10.1093/mnras/stx417

Bersten, M. C., Benvenuto, O., & Nomoto, K. 2014, in IAU Symposium, Vol. 296, Supernova Environmental Impacts, ed. A. Ray & R. A. McCray, 58–62, doi: 10.1017/S174392131300923X

Bochenek, A., Xu, D., Zhu, Z. P., et al. 2024, GRB Coordinates Network, 37039, 1

Bright, J. S., Carotenuto, F., Fender, R., et al. 2024, arXiv e-prints, arXiv:2409.19055, doi: 10.48550/arXiv.2409.19055

Buchner, J., Georgakakis, A., Nandra, K., et al. 2014, A&A, 564, A125, doi: 10.1051/0004-6361/201322971

Bufano, F., Pian, E., Sollerman, J., et al. 2012, ApJ, 753, 67, doi: 10.1088/0004-637X/753/1/67

Busmann, M., O'Connor, B., Sommer, J., et al. 2025, arXiv e-prints, arXiv:2503.14588. https://arxiv.org/abs/2503.14588

Campana, S., Mangano, V., Blustin, A. J., et al. 2006, Nature, 442, 1008, doi: 10.1038/nature04892

Cano, Z., Bersier, D., Guidorzi, C., et al. 2011, ApJ, 740, 41, doi: 10.1088/0004-637X/740/1/41

Cano, Z., Izzo, L., de Ugarte Postigo, A., et al. 2017, A&A, 605, A107, doi: 10.1051/0004-6361/201731005

Chornock, R., Berger, E., Levesque, E. M., et al. 2010, arXiv e-prints, arXiv:1004.2262, doi: 10.48550/arXiv.1004.2262

Clocchiatti, A., Suntzeff, N. B., Covarrubias, R., & Candia, P. 2011, AJ, 141, 163, doi: 10.1088/0004-6256/141/5/163

Cooke, B. A. 1976, Nature, 261, 564, doi: 10.1038/261564a0

Corsi, A., Gal-Yam, A., Kulkarni, S. R., et al. 2016, ApJ, 830, 42, doi: 10.3847/0004-637X/830/1/42

Dainotti, M. G., De Simone, B., Islam, K. M., et al. 2022, ApJ, 938, 41, doi: 10.3847/1538-4357/ac8b77

Dessart, L., Gutiérrez, C. P., Ercolino, A., Jin, H., & Langer, N. 2024, A&A, 685, A169, doi: 10.1051/0004-6361/202349066

Dessart, L., Yoon, S.-C., Aguilera-Dena, D. R., & Langer, N. 2020, A&A, 642, A106, doi: 10.1051/0004-6361/202038763

Dey, A., Schlegel, D. J., Lang, D., et al. 2019, AJ, 157, 168, doi: 10.3847/1538-3881/ab089d

Drout, M. R., Soderberg, A. M., Gal-Yam, A., et al. 2011, ApJ, 741, 97, doi: 10.1088/0004-637X/741/2/97

Evans, P. A., Beardmore, A. P., Page, K. L., et al. 2007, A&A, 469, 379, doi: 10.1051/0004-6361:20077530

—. 2009, MNRAS, 397, 1177, doi: 10.1111/j.1365-2966.2009.14913.x

Eyles-Ferris, R. A. J., Jonker, P. G., Levan, A. J., et al. 2025, arXiv e-prints, arXiv:2504.08886, doi: 10.48550/arXiv.2504.08886

Finneran, G., & Martin-Carrillo, A. 2024, arXiv e-prints, arXiv:2411.12574, doi: 10.48550/arXiv.2411.12574

Fitzpatrick, E. L. 1999, PASP, 111, 63, doi: 10.1086/316293

Flewelling, H. A., Magnier, E. A., Chambers, K. C., et al. 2020, ApJS, 251, 7, doi: 10.3847/1538-4365/abb82d

Foley, R. J., Papenkova, M. S., Swift, B. J., et al. 2003, PASP, 115, 1220, doi: 10.1086/378242

Fontana, A., Dunlop, J. S., Paris, D., et al. 2014, A&A, 570, A11, doi: 10.1051/0004-6361/201423543

Frederiks, D., Lysenko, A., Ridnaia, A., et al. 2024, GRB Coordinates Network, 37071, 1

Freudling, W., Romaniello, M., Bramich, D. M., et al. 2013, A&A, 559, A96, doi: 10.1051/0004-6361/201322494

Frey, L. H., Fryer, C. L., & Young, P. A. 2013, ApJL, 773, L7, doi: 10.1088/2041-8205/773/1/L7

Fryer, C. L. 1999, ApJ, 522, 413, doi: 10.1086/307647

Fryer, C. L., Burns, E., Ho, A. Y. Q., et al. 2024, arXiv e-prints, arXiv:2410.10378, doi: 10.48550/arXiv.2410.10378

Fryer, C. L., Fontes, C. J., Warsa, J. S., et al. 2020, ApJ, 898, 123, doi: 10.3847/1538-4357/ab99a7

Fryer, C. L., & Woosley, S. E. 1998, ApJL, 502, L9, doi: 10.1086/311493

Fryer, C. L., Keiter, P. A., Sharma, V., et al. 2023, arXiv e-prints, arXiv:2312.16677, doi: 10.48550/arXiv.2312.16677

Galama, T. J., Vreeswijk, P. M., van Paradijs, J., et al. 1998, Nature, 395, 670, doi: 10.1038/27150

Gargiulo, A., Fumana, M., Bisogni, S., et al. 2022, MNRAS, 514, 2902, doi: 10.1093/mnras/stac1065

Glennie, A., Jonker, P. G., Fender, R. P., Nagayama, T., & Pretorius, M. L. 2015, MNRAS, 450, 3765, doi: 10.1093/mnras/stv801

Greiner, J., Mazzali, P. A., Kann, D. A., et al. 2015, Nature, 523, 189, doi: 10.1038/nature14579

Grichener, A. 2025, Ap&SS, 370, 11, doi: 10.1007/s10509-025-04402-1

Groot, P. J., Bloemen, S., Vreeswijk, P. M., et al. 2024, PASP, 136, 115003, doi: 10.1088/1538-3873/ad8b6a

Harutyunyan, A. H., Pfahler, P., Pastorello, A., et al. 2008, A&A, 488, 383, doi: 10.1051/0004-6361:20078859

Heise, J., Zand, J. I., Kippen, R. M., & Woods, P. M. 2001, in Gamma-ray Bursts in the Afterglow Era, ed. E. Costa, F. Frontera, & J. Hjorth, 16, doi: 10.1007/10853853_4

Hirai, R. 2023, MNRAS, 523, 6011,
    doi: 10.1093/mnras/stad1856

Hirai, R., Podsiadlowski, P., & Yamada, S. 2018, ApJ, 864,
    119, doi: 10.3847/1538-4357/aad6a0

Hirai, R., Sato, T., Podsiadlowski, P., Vigna-Gómez, A., &
    Mandel, I. 2020, MNRAS, 499, 1154,
    doi: 10.1093/mnras/staa2898

Hiramatsu, D., Arcavi, I., Burke, J., et al. 2020, Transient
    Name Server Classification Report, 2020-403, 1

Ho, A. Y. Q., Kulkarni, S. R., Perley, D. A., et al. 2020,
    ApJ, 902, 86, doi: 10.3847/1538-4357/aba630

Hu, Y. D., Castro-Tirado, A. J., Kumar, A., et al. 2021,
    A&A, 646, A50, doi: 10.1051/0004-6361/202039349

Izzo, L., Auchettl, K., Hjorth, J., et al. 2020, A&A, 639,
    L11, doi: 10.1051/0004-6361/202038152

Izzo, L., de Ugarte Postigo, A., Maeda, K., et al. 2019,
    Nature, 565, 324, doi: 10.1038/s41586-018-0826-3

Izzo, L., Martin-Carrillo, A., Malesani, D. B., et al. 2025,
    GRB Coordinates Network, 39851, 1

Jonker, P. G., Glennie, A., Heida, M., et al. 2013, ApJ, 779,
    14, doi: 10.1088/0004-637X/779/1/14

Khatami, D. K., & Kasen, D. N. 2019, ApJ, 878, 56,
    doi: 10.3847/1538-4357/ab1f09

Labrie, K., Anderson, K., Cárdenes, R., Simpson, C., &
    Turner, J. E. H. 2019, in Astronomical Society of the
    Pacific Conference Series, Vol. 523, Astronomical Data
    Analysis Software and Systems XXVII, ed. P. J. Teuben,
    M. W. Pound, B. A. Thomas, & E. M. Warner, 321

Levan, A. J., Malesani, D. B., Jonker, P. G., et al. 2025a,
    GRB Coordinates Network, 39278, 1

Levan, A. J., Quirola-Vasquez, J. A., Rastinejad, J. C.,
    et al. 2024a, GRB Coordinates Network, 38593, 1

Levan, A. J., Rastinejad, J. C., Malesani, D. B., et al.
    2025b, GRB Coordinates Network, 38987, 1

Levan, A. J., Tanvir, N. R., Starling, R. L. C., et al. 2014,
    ApJ, 781, 13, doi: 10.1088/0004-637X/781/1/13

Levan, A. J., Jonker, P. G., Saccardi, A., et al. 2024b,
    arXiv e-prints, arXiv:2404.16350,
    doi: 10.48550/arXiv.2404.16350

Levan, A. J., Gompertz, B. P., Salafia, O. S., et al. 2024c,
    Nature, 626, 737, doi: 10.1038/s41586-023-06759-1

Li, R. Z., Chen, X. L., Chatterjee, K., et al. 2025a, GRB
    Coordinates Network, 38861, 1

Li, W. X., Zhu, Z. P., Zou, X. Z., et al. 2025b, arXiv
    e-prints, arXiv:2504.17034,
    doi: 10.48550/arXiv.2504.17034

Liljegren, S., Jerkstrand, A., Barklem, P. S., et al. 2023,
    A&A, 674, A184, doi: 10.1051/0004-6361/202243491

Lin, D., Irwin, J. A., Berger, E., & Nguyen, R. 2022, ApJ,
    927, 211, doi: 10.3847/1538-4357/ac4fc6

Liu, C., Miller, A. A., Polin, A., et al. 2023, ApJ, 946, 83,
    doi: 10.3847/1538-4357/acbb5e

Liu, Y., Sun, H., Xu, D., et al. 2025, Nature Astronomy,
    doi: 10.1038/s41550-024-02449-8

Lucy, L. B. 1991, ApJ, 383, 308, doi: 10.1086/170787

Magnier, E. A., & Cuillandre, J. C. 2004, PASP, 116, 449,
    doi: 10.1086/420756

Maguire, K., Taubenberger, S., Sullivan, M., & Mazzali,
    P. A. 2016, MNRAS, 457, 3254,
    doi: 10.1093/mnras/stv2991

Margutti, R., Metzger, B. D., Chornock, R., et al. 2019,
    ApJ, 872, 18, doi: 10.3847/1538-4357/aafa01

Matheson, T., Garnavich, P. M., Stanek, K. Z., et al. 2003,
    ApJ, 599, 394, doi: 10.1086/379228

Matzner, C. D., & McKee, C. F. 1999, ApJL, 526, L109,
    doi: 10.1086/312376

Meikle, W. P. S., Allen, D. A., Spyromilio, J., & Varani,
    G. F. 1989, MNRAS, 238, 193,
    doi: 10.1093/mnras/238.1.193

Metzger, B. D. 2019, Living Reviews in Relativity, 23, 1,
    doi: 10.1007/s41114-019-0024-0

Mirabal, N., Halpern, J. P., An, D., Thorstensen, J. R., &
    Terndrup, D. M. 2006, ApJL, 643, L99,
    doi: 10.1086/505177

Modjaz, M., Liu, Y. Q., Bianco, F. B., & Graur, O. 2016,
    ApJ, 832, 108, doi: 10.3847/0004-637X/832/2/108

Modjaz, M., Stanek, K. Z., Garnavich, P. M., et al. 2006,
    ApJL, 645, L21, doi: 10.1086/505906

Modjaz, M., Li, W., Butler, N., et al. 2009, ApJ, 702, 226,
    doi: 10.1088/0004-637X/702/1/226

Modjaz, M., Blondin, S., Kirshner, R. P., et al. 2014, AJ,
    147, 99, doi: 10.1088/0004-6256/147/5/99

Nagy, A. P. 2018, ApJ, 862, 143,
    doi: 10.3847/1538-4357/aace56

Niblett, A. E., Fryer, D. A., & Fryer, C. L. 2025, arXiv
    e-prints, arXiv:2501.15702,
    doi: 10.48550/arXiv.2501.15702

Nicholl, M., Srivastav, S., Fulton, M. D., et al. 2023, ApJL,
    954, L28, doi: 10.3847/2041-8213/acf0ba

Novara, G., Esposito, P., Tiengo, A., et al. 2020, ApJ, 898,
    37, doi: 10.3847/1538-4357/ab98f8

O'Connor, B., Pasham, D., Andreoni, I., et al. 2025, ApJL,
    979, L30, doi: 10.3847/2041-8213/ada7f5

Olivares E., F., Greiner, J., Schady, P., et al. 2012, A&A,
    539, A76, doi: 10.1051/0004-6361/201117929

Owocki, S. P., & Rybicki, G. B. 1984, ApJ, 284, 337,
    doi: 10.1086/162412

Patat, F., Cappellaro, E., Danziger, J., et al. 2001, ApJ,
    555, 900, doi: 10.1086/321526

Perley, D. A., Cenko, S. B., Corsi, A., et al. 2014, ApJ, 781, 37, doi: 10.1088/0004-637X/781/1/37

Perley, D. A., Mazzali, P. A., Yan, L., et al. 2019, MNRAS, 484, 1031, doi: 10.1093/mnras/sty3420

Pian, E., Amati, L., Antonelli, L. A., et al. 2000, ApJ, 536, 778, doi: 10.1086/308978

Pian, E., Mazzali, P. A., Masetti, N., et al. 2006, Nature, 442, 1011, doi: 10.1038/nature05082

Planck Collaboration, Aghanim, N., Akrami, Y., et al. 2020, A&A, 641, A6, doi: 10.1051/0004-6361/201833910

Prentice, S. J., Maguire, K., Smartt, S. J., et al. 2018, ApJL, 865, L3, doi: 10.3847/2041-8213/aadd90

Prochaska, J., Hennawi, J., Westfall, K., et al. 2020, The Journal of Open Source Software, 5, 2308, doi: 10.21105/joss.02308

Puls, J., Vink, J. S., & Najarro, F. 2008, A&A Rv, 16, 209, doi: 10.1007/s00159-008-0015-8

Quataert, E., Fernández, R., Kasen, D., Klion, H., & Paxton, B. 2016, MNRAS, 458, 1214, doi: 10.1093/mnras/stw365

Quirola-Vásquez, J., Bauer, F. E., Jonker, P. G., et al. 2022, A&A, 663, A168, doi: 10.1051/0004-6361/202243047

—. 2023, A&A, 675, A44, doi: 10.1051/0004-6361/202345912

Rastinejad, J. C., Gompertz, B. P., Levan, A. J., et al. 2022, Nature, 612, 223, doi: 10.1038/s41586-022-05390-w

Rastinejad, J. C., Fong, W., Levan, A. J., et al. 2024, ApJ, 968, 14, doi: 10.3847/1538-4357/ad409c

Ravasio, M. E., Burns, E., Wilson-Hodge, C., Jonker, P. G., & Fermi-GBM Team. 2025, GRB Coordinates Network, 39146, 1

Reichert, M., Obergaulinger, M., Aloy, M. Á., Gabler, M., & et al. 2023, MNRAS, 518, 1557, doi: 10.1093/mnras/stac3185

Rest, A., Stubbs, C., Becker, A. C., et al. 2005, ApJ, 634, 1103, doi: 10.1086/497060

Rodríguez, Ó., Maoz, D., & Nakar, E. 2023, ApJ, 955, 71, doi: 10.3847/1538-4357/ace2bd

Ror, A. K., Gupta, A., Kiran, Pandey, S. B., & Mishra, K. 2025, GRB Coordinates Network, 39002, 1

Sakamoto, T., Lamb, D. Q., Kawai, N., et al. 2005, ApJ, 629, 311, doi: 10.1086/431235

Santos, A., Kilpatrick, C. D., Bom, C. R., et al. 2024, MNRAS, 529, 59, doi: 10.1093/mnras/stae466

Sarin, N., Hübner, M., Omand, C. M. B., et al. 2024, MNRAS, 531, 1203, doi: 10.1093/mnras/stae1238

Schlafly, E. F., & Finkbeiner, D. P. 2011, ApJ, 737, 103, doi: 10.1088/0004-637X/737/2/103

Science Software Branch at STScI. 2012, PyRAF: Python alternative for IRAF, Astrophysics Source Code Library, record ascl:1207.011

Shahbandeh, M., Hsiao, E. Y., Ashall, C., et al. 2022, ApJ, 925, 175, doi: 10.3847/1538-4357/ac4030

Shahbandeh, M., Ashall, C., Hoeflich, P., et al. 2024, arXiv e-prints, arXiv:2401.14474, doi: 10.48550/arXiv.2401.14474

Siegel, D. M., Barnes, J., & Metzger, B. D. 2019, Nature, 569, 241, doi: 10.1038/s41586-019-1136-0

Siegel, D. M., & Metzger, B. D. 2017, PhRvL, 119, 231102, doi: 10.1103/PhysRevLett.119.231102

Skrutskie, M. F., Cutri, R. M., Stiening, R., et al. 2006, AJ, 131, 1163, doi: 10.1086/498708

Soderberg, A. M., Berger, E., Kasliwal, M., et al. 2006, ApJ, 650, 261, doi: 10.1086/506429

Soderberg, A. M., Berger, E., Page, K. L., et al. 2008, Nature, 453, 469, doi: 10.1038/nature06997

Sollerman, J., Cumming, R. J., & Lundqvist, P. 1998, ApJ, 493, 933, doi: 10.1086/305163

Song, F. F., Li, R. Z., Wang, B. T., et al. 2025, GRB Coordinates Network, 38972, 1

Srinivasaragavan, G. P., Yang, S., Anand, S., et al. 2024, ApJ, 976, 71, doi: 10.3847/1538-4357/ad7fde

Srinivasaragavan, G. P., Hamidani, H., Schroeder, G., et al. 2025, arXiv e-prints, arXiv:2504.17516, doi: 10.48550/arXiv.2504.17516

Srivastav, S., Chen, T. W., Gillanders, J. H., et al. 2025, ApJL, 978, L21, doi: 10.3847/2041-8213/ad9c75

Sun, H., Zhang, B., & Li, Z. 2015, ApJ, 812, 33, doi: 10.1088/0004-637X/812/1/33

Sun, H., Li, W. X., Liu, L. D., et al. 2024, arXiv e-prints, arXiv:2410.02315, doi: 10.48550/arXiv.2410.02315

Surman, R., McLaughlin, G. C., & Hix, W. R. 2006, ApJ, 643, 1057, doi: 10.1086/501116

Taddia, F., Sollerman, J., Fremling, C., Barbarino, C., & et al. 2019, A&A, 621, A71, doi: 10.1051/0004-6361/201834429

Tinyanont, S., Foley, R. J., Taggart, K., et al. 2024, PASP, 136, 014201, doi: 10.1088/1538-3873/ad1b39

Tonry, J. L., Denneau, L., Heinze, A. N., et al. 2018, PASP, 130, 064505, doi: 10.1088/1538-3873/aabadf

Troja, E., Fryer, C. L., O'Connor, B., et al. 2022, Nature, 612, 228, doi: 10.1038/s41586-022-05327-3

Tucker, M. A., Shappee, B. J., Vallely, P. J., et al. 2020, MNRAS, 493, 1044, doi: 10.1093/mnras/stz3390

van Dalen, J. N. D., Levan, A. J., Jonker, P. G., et al. 2025, ApJL, 982, L47, doi: 10.3847/2041-8213/adbc7e

van Dokkum, P. G. 2001, PASP, 113, 1420, doi: 10.1086/323894

Weaver, R., McCray, R., Castor, J., Shapiro, P., & Moore, R. 1977, ApJ, 218, 377, doi: 10.1086/155692

Woosley, S. E., Heger, A., & Weaver, T. A. 2002, Reviews of Modern Physics, 74, 1015, doi: 10.1103/RevModPhys.74.1015

Xiang, D., Wang, X., Lin, W., et al. 2021, ApJ, 910, 42, doi: 10.3847/1538-4357/abdeba

Xu, D., Zhu, Z. P., Liu, X., et al. 2025, GRB Coordinates Network, 38984, 1

Yan, L., Lunnan, R., Perley, D. A., et al. 2017, ApJ, 848, 6, doi: 10.3847/1538-4357/aa8993

Yang, J., Ai, S., Zhang, B.-B., et al. 2022, Nature, 612, 232, doi: 10.1038/s41586-022-05403-8

Yang, Y.-H., Becerra, R. L., Watson, A. M., et al. 2025, GRB Coordinates Network, 39305, 1

Yaron, O., & Gal-Yam, A. 2012, PASP, 124, 668, doi: 10.1086/666656

Yin, Y.-H. I., Zhang, B.-B., Yang, J., et al. 2024, ApJL, 975, L27, doi: 10.3847/2041-8213/ad8652

Yuan, W., Zhang, C., Chen, Y., & Ling, Z. 2022, in Handbook of X-ray and Gamma-ray Astrophysics, ed. C. Bambi & A. Sangangelo, 86, doi: 10.1007/978-981-16-4544-0_151-1

Yuan, W., Zhang, C., Feng, H., et al. 2015, arXiv e-prints, arXiv:1506.07735, doi: 10.48550/arXiv.1506.07735

Zenati, Y., Siegel, D. M., Metzger, B. D., & Perets, H. B. 2020, MNRAS, 499, 4097, doi: 10.1093/mnras/staa3002

Zhang, W. J., Mao, X., Zhang, W. D., et al. 2024, GRB Coordinates Network, 35931, 1

Zhu, J.-P., Liu, L.-D., Yu, Y.-W., et al. 2024, ApJL, 970, L42, doi: 10.3847/2041-8213/ad63a8

Zou, X., Liu, C., Kumar, B., et al. 2025, GRB Coordinates Network, 38914, 1

APPENDIX

6.1. *Nickel Mixing Model*

To better ascertain the quantity ^{56}Ni and to also explore the impact of mixing on our light curve fits and estimated parameters, we also fit a ^{56}Ni-mixing model. We outline the details of this model below, but detailed derivations and comparison to the one-zone model will be presented in a forthcoming publication (Sarin et al., in prep). This derivation is largely inspired by the kilonova model outlined in Metzger (2019). We begin by assuming a power-law distribution of masses under the assumption of homologous expansion

$$M_i = M_*(v_i/v_0)^{-\beta}, \tag{1}$$

where M_* is an arbitrary coefficient such that the sum of all layers is the total ejecta mass, M, v_0 is the minimum velocity of the outflow, and M_i describes the mass in each 'layer'. The number of layers is arbitrary, provided that they are sufficiently thin to accurately capture the dynamical evolution of the ejecta. A better description of SN ejecta is likely a broken power law (e.g., Matzner & McKee 1999). However, the deviations in light curve for different density profiles are smaller than the impact of mixing and other uncertain physics such as γ-ray leakage (e.g., Sollerman et al. 1998). The thermal energy of each layer evolves following the first law of thermodynamics,

$$\frac{dE_i}{dt} = \dot{Q}_i - \frac{E_i}{R_i}\frac{dR_i}{dt} - L_i. \tag{2}$$

where $\dot{Q}_i$ describes the energy input into each layer from radioactive decay, the second term on the right-hand-side describes losses due to PdV expansion and L_i describes radiative losses from each layer, which needs to account for energy losses due to the light crossing times (e.g., Metzger 2019). These equations can be numerically solved while distributing the total ^{56}Ni into layers (following the same distribution as the original mass distribution) up to a certain mass layer set by an additional parameter f_{mix} to capture nickel mixing. The photospheric radius is set as the radius of the mass shell at which the $\tau = 1$, which starts to recede back into the ejecta when the temperature drops below T_{floor}. We further improve the physics of the model by incorporating a temperature-dependent opacity following,

$$\kappa_{\mathrm{eff}} = \kappa_{\mathrm{min}} + 0.5(\kappa_{\mathrm{max}} - \kappa_{\mathrm{min}}) \times \left(1 + \tanh\left(\frac{T - T_{\mathrm{floor}}}{\Delta T}\right)\right), \tag{3}$$

where κ_{eff} is the effective opacity, which smoothly transitions from the maximum opacity, $\kappa_{\mathrm{max}} = 0.7$ cm^2 g^{-1} to the minimum opacity, $\kappa_{\mathrm{min}} = 0.07$ cm^2 g^{-1} as the temperature starts to approach T_{floor}. This functional form and ΔT are chosen to replicate the opacity evolution in detailed numerical simulations (e.g., Nagy 2018). We note that this function is merely meant to include temperature dependence and ignores the more complex dependence on density, i.e., the opacity does not vary between layers.

We fit this model to the observed light curve as we did in Section 4.1. Compared to the one-zone model, our estimated parameters better match intuition and expectations. In particular, we infer a total ejecta mass of $0.8^{+0.5}_{-0.2}$ $M_\odot$ with a ^{56}Ni mass of 0.21 ± 0.04 $M_\odot$. We also find evidence for significant mixing, with $f_{\mathrm{mix}} = 62 \pm 20\%$, that is, ^{56}Ni is distributed out into $\sim 60\%$ of the mass layers. We find the cumulative mass out to the layers with ^{56}Ni is $0.6^{+0.5}_{-0.2}M_\odot$. The lower ^{56}Ni estimate compared to our one-zone model is driven by the high mixing, which reduces the need for a larger central ^{56}Ni as the mixed material has to overcome less adiabatic losses and diffuse through less ejecta. Comparing the Bayesian evidences, we find that the mixing model is a better fit to the data, with a $\ln \mathrm{BF} = 1.4$ in favour of the mixing model.

6.2. *Priors for Modeling Near-IR Absorption Features*

We give the priors used in our fitting of the 1 and 2 μm features in Section 3.4 in Table 1.

6.3. *Tables of Observations*

Here we provide a log of the photometric programs used in this work, a lot of our spectroscopic observations, and a table of our photometric observations of SN 2025kg.

Table 1. Priors Used for Each Line Fit in Section 3.4

He I / C I / Mg II Priors	
Parameter	Prior
$\mu_v \, [\mathrm{km\,s^{-1}}]$	$\mathcal{N}(15000,\ 1000)$
$\log(\sigma_v \, [\mathrm{km\,s^{-1}}])$	$\mathcal{N}(3.5,\ 0.5)$
A	$\mathcal{U}(0,\ 5)$
$\log\left(\frac{A(2\,\mu\mathrm{m})}{A(1\,\mu\mathrm{m})}\right)$	$\mathcal{U}(-2,\ 0)$

Table 2. Photometric Programs Employed in this Work

Telescope	Instruments	Filters	Program ID(s)	P.I.(s)
BlackGEM	-	q	Local Transient Survey	-
CFHT	MegaCam	gri	K1-03-00209	A. Aryan
Gemini-North	GMOS-N	$griz$	GN-2024B-Q-107	J. Rastinejad
Gemini-South	GMOS-S, FLAMINGOS2	$grizJHK$	GS-2024B-Q-105, GS-2025A-Q-107	J. Rastinejad
LBT	MODS	$g'r'i'$	IT-2024B-023	E. Maiorano
LT	IO:O	$griz$	PL24B06, PL25A25	R. Eyles-Ferris
SLT	-	gri	–	T. Chen
NOT	ALFOSC	$griz$	70-301	P. Jonker
MMT	MMIRS	K	UAO-G206-24B	J. Rastinejad
Pan-STARRS	-	$griz$	-	S. Smartt
LOT	-	gri	R09	A. Aryan
SOAR	Goodman	riz	SOAR2024B-016	F. Bauer
T80S	T80S-Cam	$griz$	T80S-09	C. Bom, C. Kilpatrick

Table 3. Photometric Observations of SN 2025kg

Date	δt	Tel./Instum.	Band	Exp. Time	Magnitude	Ref.
	(days)			(s)	(AB mag)	
2025 Jan 14.93401	6.41285	LT/IO:O	g	6×200	21.11 ± 0.13	This work.
2025 Jan 15.21383	6.69268	Gemini-South/GMOS-S	g	60	20.94 ± 0.05	This work.
2025 Jan 15.89495	7.37379	LT/IO:O	g	6×150	20.93 ± 0.08	This work.
2025 Jan 16.47753	7.956	LOT, Lulin/Driver for Teledyne Princeton Instruments cameras	g	3×300	20.83 ± 0.11	This work.
2025 Jan 16.52491	8.00375	GMG-2.4m	g	—	20.78 ± 0.09	1
2025 Jan 16.85265	8.33149	LT/IO:O	g	4×150	20.84 ± 0.04	This work.
2025 Jan 17.87915	9.35799	LT/IO:O	g	3×150	20.81 ± 0.04	This work.
2025 Jan 17.90028	9.37911	NOT/ALFOSC	g	4×300	20.84 ± 0.03	This work.
2025 Jan 18.23900	9.71784	Pan-STARRS	g	300	20.83 ± 0.17	This work.
2025 Jan 18.83988	10.31872	LT/IO:O	g	6×120	20.67 ± 0.04	This work.

Table 3 *continued*

Table 3 *(continued)*

Date	δt	Tel./Instum.	Band	Exp. Time	Magnitude	Ref.
	(days)		(s)		(AB mag)	
2025 Jan 19.52045	10.999	SLT, Lulin/Andor CCD/EMCCD (SDK2)	g	18×300	20.92 ± 0.24	This work.
2025 Jan 19.82822	11.30706	LT/IO:O	g	6×100	20.68 ± 0.06	This work.
2025 Jan 19.91938	11.39821	NOT/ALFOSC	g	2×300	20.67 ± 0.03	This work.
2025 Jan 20.24500	11.72384	Pan-STARRS	g	400	20.65 ± 0.10	This work.
2025 Jan 22.09702	13.57586	LCO/Sinistro	g	3×300	20.47 ± 0.05	This work.
2025 Jan 22.19166	13.671	LBT/MODS	g	3×120	20.39 ± 0.02	This work.
2025 Jan 22.23900	13.71784	Pan-STARRS	g	300	20.56 ± 0.09	This work.
2025 Jan 23.093	14.57184	T80S/T80S-Cam	g	180	20.73 ± 0.19	This work.
2025 Jan 23.09692	14.57576	T80S/T80S-Cam	g	180	20.77 ± 0.28	This work.
2025 Jan 23.10191	14.58075	LCO/Sinistro	g	3×300	20.60 ± 0.04	This work.
2025 Jan 24.17622	15.65506	LCO/Sinistro	g	3×300	20.51 ± 0.04	This work.
2025 Jan 24.25	15.72884	Pan-STARRS	g	300	20.69 ± 0.15	This work.
2025 Jan 25.83566	17.3145	LT/IO:O	g	2×60	20.72 ± 0.12	This work.
2025 Jan 26.23599	17.71484	Pan-STARRS	g	300	20.61 ± 0.13	This work.
2025 Jan 26.83535	18.31419	LT/IO:O	g	6×100	20.62 ± 0.04	This work.
2025 Jan 27.06368	18.54252	T80S/T80S-Cam	g	180	20.83 ± 0.15	This work.
2025 Jan 27.06768	18.54652	T80S/T80S-Cam	g	180	20.94 ± 0.16	This work.
2025 Jan 27.8232	19.30204	LT/IO:O	g	6×100	20.90 ± 0.11	This work.
2025 Jan 28.83482	20.31366	LT/IO:O	g	6×100	20.82 ± 0.05	This work.
2025 Jan 29.07637	20.55521	T80S/T80S-Cam	g	180	21.11 ± 0.22	This work.
2025 Jan 29.0803	20.55914	T80S/T80S-Cam	g	180	21.06 ± 0.21	This work.
2025 Jan 29.29000	20.76884	Pan-STARRS	g	300	20.88 ± 0.07	This work.
2025 Jan 29.83971	21.31854	NOT/ALFOSC	g	2×300	20.83 ± 0.04	This work.
2025 Jan 30.05121	21.53005	T80S/T80S-Cam	g	180	21.33 ± 0.27	This work.
2025 Jan 30.05526	21.5341	T80S/T80S-Cam	g	180	21.27 ± 0.23	This work.
2025 Feb 3.87949	26.35832	NOT/ALFOSC	g	3×300	21.27 ± 0.04	This work.
2025 Feb 05.23099	27.70984	Pan-STARRS	g	300	> 21.18	This work.
2025 Feb 8.86684	31.34567	NOT/ALFOSC	g	4×300	21.72 ± 0.11	This work.
2025 Feb 16.15225	36.6311	ZTF	g	30	> 21.77	This work.
2025 Feb 21.23332	43.712	CFHT/MegaCam	g	1×60	22.34 ± 0.13	This work.
2025 Mar 16.00208	66.48091	Gemini-South/GMOS-S	g	7×120	22.75 ± 0.06	This work.
2025 Jan 19.08561	10.56445	BlackGEM	q	60	20.51 ± 0.12	This work.
2025 Jan 22.08465	13.5635	BlackGEM	q	60	20.20 ± 0.11	This work.
2025 Jan 23.08454	14.56339	BlackGEM	q	60	19.93 ± 0.09	This work.
2025 Jan 24.10005	15.57889	BlackGEM	q	60	20.35 ± 0.11	This work.
2025 Jan 25.08014	16.55898	BlackGEM	q	60	20.12 ± 0.10	This work.
2025 Jan 26.07680	17.55565	BlackGEM	q	60	20.38 ± 0.12	This work.
2025 Jan 27.07300	18.55185	BlackGEM	q	60	20.31 ± 0.11	This work.
2025 Jan 15.17612	6.65497	Gemini-South/GMOS-S	r	100	20.68 ± 0.12	This work.
2025 Jan 15.60866	7.0875	GMG-2.4m	r	—	20.75 ± 0.16	1
2025 Jan 15.90684	7.38568	LT/IO:O	r	6×150	20.53 ± 0.05	This work.
2025 Jan 16.26299	7.74184	Pan-STARRS	r	300	20.41 ± 0.17	This work.
2025 Jan 16.46645	7.945	LOT, Lulin/Driver for Teledyne Princeton Instruments cameras	r	3×300	20.55 ± 0.07	This work.
2025 Jan 16.52824	8.00708	GMG-2.4m	r	—	20.28 ± 0.07	1
2025 Jan 16.86631	8.34515	LT/IO:O	r	5×150	20.45 ± 0.06	This work.

Table 3 *continued*

Rastinejad et al.

Table 3 *(continued)*

Date	δt	Tel./Instum.	Band	Exp. Time	Magnitude	Ref.
	(days)		(s)		(AB mag)	
2025 Jan 17.89496	9.3738	LT/IO:O	r	7 × 150	20.39 ± 0.03	This work.
2025 Jan 17.91044	9.38927	NOT/ALFOSC	r	2 × 180	20.30 ± 0.03	This work.
2025 Jan 18.24299	9.72184	Pan-STARRS	r	300	20.32 ± 0.15	This work.
2025 Jan 18.84968	10.32852	LT/IO:O	r	6 × 120	20.30 ± 0.06	This work.
2025 Jan 19.05309	10.53194	Gemini-South/GMOS-S	r	60	20.31 ± 0.05	This work.
2025 Jan 19.1257	10.60454	T80S/T80S-Cam	r	180	20.31 ± 0.15	This work.
2025 Jan 19.12961	10.60845	T80S/T80S-Cam	r	180	20.45 ± 0.19	This work.
2025 Jan 19.48267	10.962	LOT, Lulin/Driver for Teledyne Princeton Instruments cameras	r	6 × 300	20.24 ± 0.06	This work.
2025 Jan 19.83732	11.31616	LT/IO:O	r	5 × 100	20.20 ± 0.04	This work.
2025 Jan 19.92580	11.40463	NOT/ALFOSC	r	2 × 180	20.25 ± 0.03	This work.
2025 Jan 20.24900	11.72784	Pan-STARRS	r	300	20.21 ± 0.06	This work.
2025 Jan 22.03038	13.50923	Gemini-South/GMOS-S	r	60	20.15 ± 0.12	This work.
2025 Jan 22.09848	13.57732	T80S/T80S-Cam	r	180	20.21 ± 0.16	This work.
2025 Jan 22.10085	13.57969	LCO/Sinistro	r	3 × 300	20.12 ± 0.04	This work.
2025 Jan 22.10241	13.58125	T80S/T80S-Cam	r	180	20.23 ± 0.16	This work.
2025 Jan 22.19305	13.672	LBT/MODS	r	6 × 120	20.12 ± 0.01	This work.
2025 Jan 22.24299	13.72184	Pan-STARRS	r	300	20.09 ± 0.08	This work.
2025 Jan 23.07442	14.55327	Gemini-South/GMOS-S	r	60	20.15 ± 0.10	This work.
2025 Jan 23.101	14.57984	T80S/T80S-Cam	r	180	20.26 ± 0.15	This work.
2025 Jan 23.10493	14.58377	T80S/T80S-Cam	r	180	20.21 ± 0.13	This work.
2025 Jan 23.10575	14.58459	LCO/Sinistro	r	3 × 300	20.09 ± 0.04	This work.
2025 Jan 24.18007	15.65891	LCO/Sinistro	r	3 × 300	20.06 ± 0.05	This work.
2025 Jan 24.25400	15.73284	Pan-STARRS	r	300	19.99 ± 0.10	This work.
2025 Jan 25.05144	16.53028	Gemini-South/GMOS-S	r	60	20.08 ± 0.14	This work.
2025 Jan 25.83161	17.31045	LT/IO:O	r	12 × 60	20.21 ± 0.09	This work.
2025 Jan 26.06544	17.54428	T80S/T80S-Cam	r	180	20.20 ± 0.10	This work.
2025 Jan 26.23999	17.71884	Pan-STARRS	r	300	20.06 ± 0.10	This work.
2025 Jan 26.84378	18.32262	LT/IO:O	r	6 × 100	20.07 ± 0.05	This work.
2025 Jan 27.07169	18.55053	T80S/T80S-Cam	r	180	20.22 ± 0.10	This work.
2025 Jan 27.07566	18.5545	T80S/T80S-Cam	r	180	20.18 ± 0.09	This work.
2025 Jan 27.08282	18.56598	SOAR/Goodman	r	5 × 140	20.11 ± 0.02	This work.
2025 Jan 27.83161	19.31045	LT/IO:O	r	6 × 100	20.12 ± 0.04	This work.
2025 Jan 28.14083	19.61968	Gemini-South/GMOS-S	r	60	20.16 ± 0.12	This work.
2025 Jan 28.84324	20.32208	LT/IO:O	r	6 × 100	20.17 ± 0.03	This work.
2025 Jan 29.08431	20.56315	T80S/T80S-Cam	r	180	20.33 ± 0.10	This work.
2025 Jan 29.08825	20.56709	T80S/T80S-Cam	r	180	20.29 ± 0.10	This work.
2025 Jan 29.24197	20.72082	Gemini-North/GMOS-N	r	50	20.17 ± 0.07	This work.
2025 Jan 29.29400	20.77284	Pan-STARRS	r	300	20.06 ± 0.05	This work.
2025 Jan 29.84613	21.32497	NOT/ALFOSC	r	2 × 180	20.20 ± 0.02	This work.
2025 Jan 30.0593	21.53814	T80S/T80S-Cam	r	180	20.24 ± 0.10	This work.
2025 Jan 30.0633	21.54214	T80S/T80S-Cam	r	180	20.31 ± 0.11	This work.
2025 Feb 3.89605	26.37488	NOT/ALFOSC	r	2 × 180	20.44 ± 0.03	This work.
2025 Feb 05.23400	27.71284	Pan-STARRS	r	300	20.47 ± 0.24	This work.
2025 Feb 8.87705	31.35588	NOT/ALFOSC	r	2 × 180	20.77 ± 0.06	This work.
2025 Feb 19.11887	40.59772	ZTF	r	30	> 21.09	This work.

Table 3 *continued*

Table 3 *(continued)*

Date	δt	Tel./Instum.	Band	Exp. Time	Magnitude	Ref.
	(days)		(s)		(AB mag)	
2025 Feb 18.44954	40.928	LOT, Lulin/Driver for Teledyne Princeton Instruments cameras	r	6×300	21.43 ± 0.10	This work.
2025 Feb 20.01365	42.49249	Gemini-South/GMOS-S	r	60	21.59 ± 0.12	This work.
2025 Feb 21.22865	43.708	CFHT/MegaCam	r	3×60	21.66 ± 0.08	This work.
2025 Feb27.83787	50.31671	NOT/ALFOSC	r	4×180	21.90 ± 0.07	This work.
2025 Mar 16.01389	66.49272	Gemini-South/GMOS-S	r	7×120	22.19 ± 0.07	This work.
2025 Jan 19.67752	11.15636	DFOT	R	12×300	19.89 ± 0.04	This work.
2025 Jan 15.44627	6.92512	ATLAS	o	7×30	> 19.70	This work.
2025 Jan 16.85751	8.33636	ATLAS	o	4×30	20.00 ± 0.21	This work.
2025 Jan 18.09971	9.57855	ATLAS	o	4×30	> 19.90	This work.
2025 Jan 19.86149	11.34034	ATLAS	o	4×30	> 20.27	This work.
2025 Jan 20.87214	12.35098	ATLAS	o	4×30	> 19.84	This work.
2025 Jan 23.86630	15.34515	ATLAS	o	3×30	19.99 ± 0.20	This work.
2025 Jan 24.83415	16.313	ATLAS	o	4×30	20.09 ± 0.17	This work.
2025 Jan 28.83719	20.31603	ATLAS	o	4×30	> 20.05	This work.
2025 Feb 01.80872	24.28757	ATLAS	o	4×30	20.17 ± 0.21	This work.
2025 Feb 04.46553	26.94438	ATLAS	o	8×30	20.23 ± 0.19	This work.
2025 Jan 15.22278	6.70162	Gemini-South/GMOS-S	i	60	20.95 ± 0.07	This work.
2025 Jan 15.9187	7.39754	LT/IO:O	i	6×150	20.81 ± 0.04	This work.
2025 Jan 16.26700	7.74584	Pan-STARRS	i	300	20.86 ± 0.23	This work.
2025 Jan 16.45980	7.939	SLT, Lulin/Andor CCD/EMCCD (SDK2)	i	24×300	> 19.80	This work.
2025 Jan 16.87837	8.35721	LT/IO:O	i	6×150	20.63 ± 0.04	This work.
2025 Jan 17.51716	8.996	SLT, Lulin/Andor CCD/EMCCD (SDK2)	i	35×300	20.55 ± 0.21	This work.
2025 Jan 17.90765	9.38649	LT/IO:O	i	5×150	20.38 ± 0.06	This work.
2025 Jan 17.91660	9.39543	NOT/ALFOSC	i	3×180	20.50 ± 0.04	This work.
2025 Jan 18.24700	9.72584	Pan-STARRS	i	300	20.48 ± 0.15	This work.
2025 Jan 18.85947	10.33831	LT/IO:O	i	6×120	20.40 ± 0.04	This work.
2025 Jan 19.13363	10.61247	T80S/T80S-Cam	i	180	20.60 ± 0.27	This work.
2025 Jan 19.13759	10.61643	T80S/T80S-Cam	i	180	20.66 ± 0.27	This work.
2025 Jan 19.84502	11.32386	LT/IO:O	i	6×100	20.30 ± 0.03	This work.
2025 Jan 19.93194	11.41078	NOT/ALFOSC	i	3×180	20.38 ± 0.03	This work.
2025 Jan 20.25299	11.73184	Pan-STARRS	i	300	20.42 ± 0.13	This work.
2025 Jan 22.10646	13.5853	T80S/T80S-Cam	i	180	20.43 ± 0.19	This work.
2025 Jan 22.11039	13.58923	T80S/T80S-Cam	i	180	20.45 ± 0.17	This work.
2025 Jan 22.19444	13.673	LBT/MODS	i	6×120	20.28 ± 0.02	This work.
2025 Jan 22.24599	13.72484	Pan-STARRS	i	300	20.29 ± 0.10	This work.
2025 Jan 23.10904	14.58788	T80S/T80S-Cam	i	180	20.32 ± 0.15	This work.
2025 Jan 23.10961	14.58845	LCO/Sinistro	i	3×300	20.19 ± 0.06	This work.
2025 Jan 23.11296	14.5918	T80S/T80S-Cam	i	180	20.48 ± 0.20	This work.
2025 Jan 23.50364	14.982	SLT, Lulin/Andor CCD/EMCCD (SDK2)	i	36×300	20.36 ± 0.14	This work.
2025 Jan 24.10162	15.59028	SOAR/Goodman	i	12×120	20.17 ± 0.01	This work.
2025 Jan 24.18393	15.66277	LCO/Sinistro	i	3×300	20.13 ± 0.07	This work.
2025 Jan 24.25799	15.73684	Pan-STARRS	i	300	20.09 ± 0.16	This work.
2025 Jan 25.83837	17.31721	LT/IO:O	i	12×100	20.14 ± 0.05	This work.
2025 Jan 26.07339	17.55223	T80S/T80S-Cam	i	180	20.85 ± 0.19	This work.
2025 Jan 26.24299	17.72184	Pan-STARRS	i	300	20.23 ± 0.14	This work.

Table 3 *continued*

Rastinejad et al.

Table 3 *(continued)*

Date	δt	Tel./Instum.	Band	Exp. Time	Magnitude	Ref.
	(days)		(s)	(AB mag)		
2025 Jan 26.85217	18.33101	LT/IO:O	i	6×100	20.15 ± 0.04	This work.
2025 Jan 27.07968	18.55852	T80S/T80S-Cam	i	180	20.27 ± 0.11	This work.
2025 Jan 27.08373	18.56257	T80S/T80S-Cam	i	180	20.33 ± 0.11	This work.
2025 Jan 27.84	19.31884	LT/IO:O	i	6×100	20.12 ± 0.03	This work.
2025 Jan 28.85165	20.33049	LT/IO:O	i	6×100	20.20 ± 0.03	This work.
2025 Jan 29.09227	20.57111	T80S/T80S-Cam	i	180	20.56 ± 0.16	This work.
2025 Jan 29.0962	20.57504	T80S/T80S-Cam	i	180	20.37 ± 0.13	This work.
2025 Jan 29.29799	20.77684	Pan-STARRS	i	300	20.26 ± 0.07	This work.
2025 Jan 29.85230	21.33113	NOT/ALFOSC	i	3×180	20.28 ± 0.03	This work.
2025 Jan 30.06734	21.54618	T80S/T80S-Cam	i	180	20.62 ± 0.18	This work.
2025 Jan 30.07129	21.55013	T80S/T80S-Cam	i	180	20.61 ± 0.18	This work.
2025 Feb 3.90219	26.38102	NOT/ALFOSC	i	3×180	20.38 ± 0.04	This work.
2025 Feb 05.23799	27.71684	Pan-STARRS	i	300	> 20.67	This work.
2025 Feb 8.88318	31.36201	NOT/ALFOSC	i	3×180	20.59 ± 0.07	This work.
2025 Feb 21.23631	43.715	CFHT/MegaCam	i	5×60	21.35 ± 0.08	This work.
2026 Feb27.84760	50.32644	NOT/ALFOSC	i	3×360	21.54 ± 0.06	This work.
2025 Mar 16.02813	66.50699	Gemini-South/GMOS-S	i	7×100	22.04 ± 0.09	This work.
2025 Jan 14.96824	6.44708	LT/IO:O	z	6×200	21.06 ± 0.18	This work.
2025 Jan 15.22722	6.70606	Gemini-South/GMOS-S	z	60	21.25 ± 0.14	This work.
2025 Jan 15.93347	7.41231	LT/IO:O	z	6×250	20.82 ± 0.09	This work.
2025 Jan 16.27099	7.74984	Pan-STARRS	z	300	> 20.82	This work.
2025 Jan 16.89159	8.37043	LT/IO:O	z	3×250	21.07 ± 0.12	This work.
2025 Jan 17.92261	9.40145	LT/IO:O	z	6×250	20.89 ± 0.10	This work.
2025 Jan 17.92701	9.40584	NOT/ALFOSC	z	5×200	21.03 ± 0.10	This work.
2025 Jan 18.25	9.72884	Pan-STARRS	z	400	> 21.01	This work.
2025 Jan 18.8703	10.34914	LT/IO:O	z	5×200	20.74 ± 0.12	This work.
2025 Jan 19.85485	11.33369	LT/IO:O	z	6×150	20.80 ± 0.07	This work.
2025 Jan 19.94758	11.42641	NOT/ALFOSC	z	9×200	20.85 ± 0.07	This work.
2025 Jan 20.25700	11.73584	Pan-STARRS	z	400	20.69 ± 0.23	This work.
2025 Jan 22.25	13.72884	Pan-STARRS	z	400	20.66 ± 0.19	This work.
2025 Jan 23.11703	14.59587	T80S/T80S-Cam	z	180	> 21.14	This work.
2025 Jan 23.12095	14.59979	T80S/T80S-Cam	z	180	20.57 ± 0.24	This work.
2025 Jan 24.05224	15.54025	SOAR/Goodman	z	12×120	20.43 ± 0.03	This work.
2025 Jan 24.26099	15.73984	Pan-STARRS	z	400	> 20.55	This work.
2025 Jan 25.85688	17.33572	LT/IO:O	z	6×100	20.68 ± 0.13	This work.
2025 Jan 26.07752	17.55636	T80S/T80S-Cam	z	180	20.19 ± 0.18	This work.
2025 Jan 26.08148	17.56032	T80S/T80S-Cam	z	180	20.64 ± 0.29	This work.
2025 Jan 26.24700	17.72584	Pan-STARRS	z	400	20.60 ± 0.28	This work.
2025 Jan 26.86055	18.33939	LT/IO:O	z	6×100	20.39 ± 0.09	This work.
2025 Jan 27.08774	18.56658	T80S/T80S-Cam	z	180	20.46 ± 0.21	This work.
2025 Jan 27.84839	19.32723	LT/IO:O	z	6×100	20.54 ± 0.10	This work.
2025 Jan 28.86005	20.33889	LT/IO:O	z	6×100	20.56 ± 0.08	This work.
2025 Jan 29.10028	20.57912	T80S/T80S-Cam	z	180	20.45 ± 0.25	This work.
2025 Jan 29.30099	20.77984	Pan-STARRS	z	400	20.36 ± 0.21	This work.
2025 Jan 29.86795	21.34678	NOT/ALFOSC	z	9×200	20.56 ± 0.09	This work.

Table 3 *continued*

Date	δt	Tel./Instum.	Band	Exp. Time	Magnitude	Ref.
	(days)		(s)		(AB mag)	
2025 Jan 30.07532	21.55416	T80S/T80S-Cam	z	180	20.29 ± 0.24	This work.
2025 Feb 3.91785	26.39668	NOT/ALFOSC	z	9×200	20.66 ± 0.08	This work.
2025 Feb 05.24200	27.72084	Pan-STARRS	z	400	> 20.35	This work.
2025 Feb 8.89881	31.37764	NOT/ALFOSC	z	9×200	20.94 ± 0.09	This work.
2025 Feb 10.27033	32.74917333	Pan-STARRS	z	1800	20.85 ± 0.22	This work.
2025 Feb 14.24841	36.72725667	Pan-STARRS	z	1800	21.00 ± 0.06	This work.
2025 Feb 21.23366	43.71250667	Pan-STARRS	z	1800	21.55 ± 0.23	This work.
2027 Feb27.86133	50.34017	NOT/ALFOSC	z	5×300	21.56 ± 0.21	This work.
2025 Mar 01.24099	51.71984	Pan-STARRS	z	1800	21.74 ± 0.33	This work.
2025 Mar 16.23999	66.71884	Pan-STARRS	z	1800	> 21.41	This work.
2025 Jan 20.03253	11.51137	Gemini-South/F2	J	26×30	20.76 ± 0.03	This work.
2025 Jan 29.10275	20.58159	Gemini-South/F2	J	25×30	20.61 ± 0.06	This work.
2025 Jan 20.05285	11.53169	Gemini-South/F2	H	38×10	21.25 ± 0.11	This work.
2025 Jan 23.08603	14.56486	Gemini-South/F2	H	10×10	21.22 ± 0.12	This work.
2025 Jan 25.08371	16.56255	Gemini-South/F2	H	32×10	21.09 ± 0.12	This work.
2025 Jan 28.08175	19.56059	Gemini-South/F2	H	22×10	21.21 ± 0.11	This work.
2025 Feb 09.12099	31.59983	Gemini-South/F2	H	66×10	21.20 ± 0.13	This work.
2025 Feb 22.01750	44.49633	Gemini-South/F2	H	38×10	21.76 ± 0.12	This work.
2025 Mar 08.00869	58.48752	Gemini-South/F2	H	41×10	22.25 ± 0.19	This work.
2025 Jan 20.14749	11.62633	MMT/MMIRS	K	93×20	21.45 ± 0.15	This work.
2025 Jan 29.11899	20.59782	Gemini-South/F2	K	38×10	21.02 ± 0.07	This work.

NOTE— Observations are not corrected for Galactic nor local extinction.

Times are presented in the observer frame.

References: (1) Song et al. (2025)

Table 4. Log of SN 2025kg Spectroscopic Observations

Date & Mid-Time	δt	Tel.	Instrum.	Exp. Time	Wavelength Range
(UTC)	(days)			(s)	(Å)
2025-01-19 01:41:47	10.5	Gemini-South	GMOS	4×400	$4300 - 8400$
2025-01-19 07:42:41	10.8	Gemini-North	GMOS	4×1200	$4800 - 9000$
2025-01-19 21:17:24	11.4	GTC	OSIRIS	$3 \times 1200, 3 \times 900$	$3600 - 9500$
2025-01-22 01:12:58	13.5	Gemini-South	GMOS	4×250	$4300 - 9000$
2025-01-22 04:10:00	13.7	LBT	MODS	2×900	$3200 - 10000$
2025-01-22 05:57:25	13.7	Gemini-North	GNIRS	11×300	$7000 - 21400$
2025-01-24 02:25:46	15.6	VLT	MUSE	4×608	$4700 - 9300$
2025-01-25 01:35:30	16.5	Gemini-South	GMOS	4×400	$4300 - 8400$
2025-01-25 16:43:34	17.2	JWST	NIRSpec	6302.4	$6000 - 53000$
2025-01-26 05:45:45	17.7	Keck I	LRIS	3×900	$3000 - 10200$
2025-01-29 06:25:50	20.7	Gemini-South	GMOS	4×800	$4900 - 9400$
2025-01-29 05:25:51	20.7	Keck I	LRIS	2×900	$3000 - 10200$
2025-02-05 21:02:32	28.4	GTC	OSIRIS	3×900	$3200 - 9400$
2025-02-20 01:14:56	42.5	Gemini-South	GMOS	4×800	$5500 - 9400$
2025-02-26 05:57:25	47.4	Keck I	LRIS	3×1200	$3000 - 8900$